https://doi.org/10.5194/egusphere-2026-2725
Preprint. Discussion started: 27 May 2026

Combined assimilation of Sentinel-2 snow cover fraction and snow station data improves fully distributed snow simulation across multiple spatial scales

Moritz Oberrauch[1,2], Bertrand Cluzet[1], Jan Magnusson[1], Gabriele Schwaizer[3], and Tobias Jonas[1]

[1]WSL Institute for Snow and Avalanche Research SLF, Davos, Switzerland
[2]Department of Civil, Environmental and Geomatic Engineering, ETH Zürich, Switzerland
[3]ENVEO - Environmental Earth Observation IT GmbH, Innsbruck, Austria

Correspondence: Moritz Oberrauch (moritz.oberrauch@slf.ch)

Abstract. Seasonal snow cover and meltwater runoff have wide-ranging ecological, hydrological, and socioeconomic effects on regions within and downstream of mountainous areas, underscoring the need for accurate monitoring. Snow data assimilation improves estimates of snowpack evolution by combining numerical simulations with observational data, as neither source alone can adequately capture the strong spatial and temporal variability of mountain snowpacks. However, the benefit of assimilating spatially sparse or temporally infrequent observations is maximized only when these observations are representative of unobserved areas and unmonitored periods. In this study, we present a novel two-step framework for the combined assimilation of in situ snow depth observations and spaceborne snow cover fraction (SCF) observations. First, a particle filter–based assimilation of point-scale snow depth observations accounts for spatiotemporal uncertainties in the meteorological forcing at subregional scales over consecutive three-day assimilation windows. Second, the remaining small-scale errors are addressed by assimilating SCF maps using a particle batch smoother, targeting grid-cell-specific uncertainties in model parameters that control the representation of albedo decay and gravitational redistribution within the model. These parameters explicitly address deviations in snowpack evolution related to slope and aspect relative to the flat-field locations, and are therefore independent of the forcing corrections inferred during the first assimilation step. The proposed approach reduces the RMSE and bias of SCF estimates during the ablation season by approximately 50 % at observed locations. At unobserved locations, estimates are updated by interpolating the inferred parameters based on horizontal distance and terrain differences, yielding considerable albeit less pronounced improvements. Overall, this study demonstrates that assimilating complementary snow observations can substantially improve near-real-time snowpack simulations across multiple spatial scales over complex mountainous terrain.

1 Introduction

Seasonal snow is an integral part of the hydrological cycle in high-latitude and mountainous regions, serving as a natural water reservoir (DeWalle and Rango, 2008; Immerzeel et al., 2020). Snow cover duration as well as the timing and magnitude of meltwater runoff have wide-ranging ecological and socioeconomic effects, including impacts on flora and fauna (Slatyer et al., 2022), freshwater availability (Siirila-Woodburn et al., 2021), hydropower production (Magnusson et al., 2020), agriculture

https://doi.org/10.5194/egusphere-2026-2725
Preprint. Discussion started: 27 May 2026

(Qin et al., 2020), winter tourism (Morin et al., 2021), and the risk of natural hazards such as avalanches (Eckert et al., 2024) and snowmelt-driven floods (Musselman et al., 2018). Hence, it is crucial to accurately estimate seasonal snow accumulation and ablation, particularly under changing climatic conditions (Barnett et al., 2005; Beniston et al., 2018; Hock et al., 2022).

The mountain snowpack exhibits pronounced spatial heterogeneity due to variations in accumulation and ablation patterns across all scales, making it particularly challenging to quantify (Blöschl, 1999; Clark et al., 2011; Dozier et al., 2016). This heterogeneity arises from interactions between atmospheric processes and complex terrain, including preferential deposition, wind- and gravity-driven redistribution, and other small-scale micrometeorological effects that strongly shape the spatial distribution of snow cover (López-Moreno et al., 2013; Sommer et al., 2015; Grünewald et al., 2010; Mott et al., 2018; Quéno et al., 2024). In situ observations of bulk snowpack properties, such as snow depth and snow water equivalent (SWE), are typically too sparse to accurately characterize this spatial variability (Dozier et al., 2016; Largeron et al., 2020), given their inherently limited representativeness of the surrounding terrain (Grünewald and Lehning, 2015). Complementary spatially distributed information can be obtained from remotely sensed snow observations, with spaceborne platforms providing coverage over large spatial extents (e.g., Gascoin et al., 2019; Lievens et al., 2022). However, such observations can be limited by accuracy, spatial resolution, infrequent revisit times, reliance on daylight and cloud-free conditions for optical sensors, and other retrieval uncertainties over complex and steep terrain (Tsang et al., 2022; Gascoin et al., 2024). Numerical models, in turn, provide continuous estimates of snowpack evolution in space and time. Still, their outputs are inherently uncertain due to the necessary parametrization of physical processes and errors in atmospheric forcing (Günther et al., 2019, 2020; Menard et al., 2021).

Data assimilation (DA) merges numerical simulations with observational data to yield more robust state estimates (e.g., Carrassi et al., 2018) and has become an increasingly common tool in snow modeling (Helmert et al., 2018; Girotto et al., 2020; Largeron et al., 2020; Alonso-González et al., 2022). Multiple studies have shown that assimilating in situ observations substantially improves estimates of snow depth, SWE, and snow density, directly at the observation locations (Magnusson et al., 2017; Smyth et al., 2019; Piazzi et al., 2019), but also over large domains and for operational applications (Winstral et al., 2019; Cantet et al., 2019; Cluzet et al., 2022; Oberrauch et al., 2024) using different methods to propagate information to unobserved areas. For example, Alonso-González et al. (2023) demonstrated that multidimensional topographic correlations within a small mountainous catchment can be leveraged to propagate information and improve distributed snowpack estimates when assimilating sparse, high-accuracy snow depth observations. Furthermore, it was shown that assimilating a single spatially distributed snow depth map, whether from airborne lidar observations (Margulis et al., 2019) or spaceborne stereoscopic imagery (Deschamps-Berger et al., 2022), can improve snow depth and SWE estimates throughout the entire season. However, such distributed datasets are generally available only for smaller, selected regions (e.g., Marti et al., 2016; Bühler et al., 2015; Bührle et al., 2023), with the exception of a growing number of catchments in the US (Painter et al., 2016).

Several studies have explored the assimilation of spaceborne snow observations spanning large spatial extents, such as reflectance data from MODIS and Sentinel-2 (Charrois et al., 2016; Cluzet et al., 2020; Revuelto et al., 2021), or snow depth retrievals from Sentinel-1 (Lievens et al., 2022; Girotto et al., 2024) and ICESat-2 lidar (Mazzolini et al., 2025). Although the potential of such approaches has been demonstrated, the availability and uncertainty of these data still limit their broader use, particularly for operational applications (De Lannoy et al., 2022). In contrast, assimilating spaceborne snow cover fraction

https://doi.org/10.5194/egusphere-2026-2725
Preprint. Discussion started: 27 May 2026

(SCF) observations, often via Ensemble Smoother techniques (e.g., Girotto et al., 2014b; Margulis et al., 2015; Aalstad et al., 2018), is widely employed in snow reanalysis systems (e.g., Girotto et al., 2014a; Margulis et al., 2016; Baba et al., 2018; Fiddes et al., 2019; Alonso-González et al., 2021; Liu et al., 2021). In this context, the seasonal evolution of the snowpack can be reconstructed from the observed snow disappearance (Girotto et al., 2014b), given that SCF observations contain the most information during periods of partial snow cover. However, despite the information in SCF observations generally being limited to the early-season accumulation and late-season ablation periods, there are potential benefits to sequentially assimilating SCF observations (Baba et al., 2018). In particular, SCF can complement sparse in situ monitoring networks by capturing the spatial heterogeneity of the mountain snowpack, which is not detectable from point-based observations (Cluzet et al., 2024; Oberrauch et al., 2025).

To integrate spaceborne SCF observations into an operational nowcasting application, we propose a two-step assimilation scheme that incorporates point-based snow depth measurements and spatial SCF observations into the distributed, physics-based, multi-layer snow model FSM2OSHD (Mott et al., 2023). In a first step, the particle-filter-based assimilation of in situ snow depth observations (Oberrauch et al., 2024) corrects errors in the meteorological forcing data at a subregional scale. However, the information content of point observations from flat-field locations is limited and does not allow addressing uncertainties in model parameterizations that govern small-scale accumulation and ablation patterns, as evidenced by comparisons with SCF observations derived from Sentinel-2 retrievals (Cluzet et al., 2024; Oberrauch et al., 2025). Hence, in a second step, these corrected forcings are used to drive local ensemble simulations at each grid cell, while explicitly perturbing model parameters that control aspect- and slope-dependent processes that modulate snow accumulation and ripening relative to flat fields. A Particle Batch Smoother is then used to assimilate multiple high-resolution SCF observations over the course of the season, thereby estimating optimal model parameters for all observable grid cells, which are subsequently interpolated to unobserved locations.

In this study, we describe and evaluate the proposed two-step assimilation framework, with particular emphasis on the second step, namely the assimilation of SCF maps to estimate optimal model parameters. We first illustrate the progressive improvements in modeled snow-cover patterns as the two assimilation steps are applied. We then quantify the improvements from assimilating SCF observations at both observed and unobserved grid cells and evaluate the sensitivity of the results to the interpolation settings. Finally, we assess how the proposed approach can be integrated into an operational framework for near-real-time estimation of snowpack evolution across large mountainous regions.

2 Methods

2.1 Study area

The study domain comprises Switzerland and its hydrologically connected bordering regions (Figure 1, top center). Covering more than 58,000 km^2 and spanning elevations from 180 m to 4750 m, it was selected to ensure national-scale applicability for operational use across a wide range of climatic and topographic conditions. For better illustration, the results are presented in

https://doi.org/10.5194/egusphere-2026-2725
Preprint. Discussion started: 27 May 2026

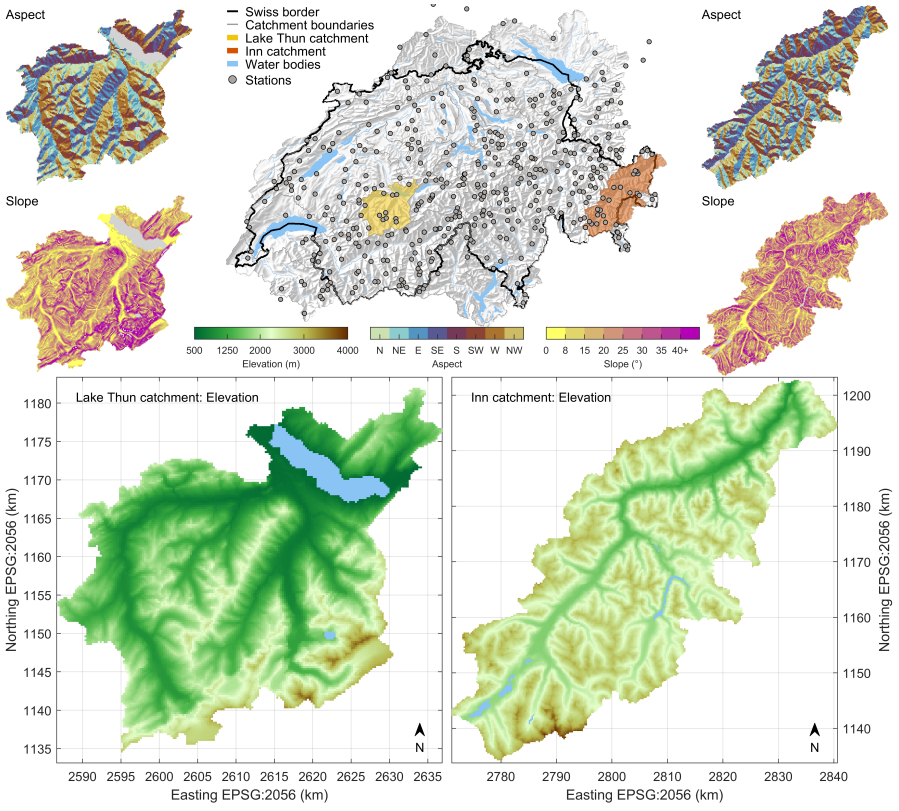

Figure 1. Overview of the study domain and topographic parameters. The top central map illustrates the model domain covering Switzerland and hydrologically connected bordering regions, showing the Swiss border as a black line, the snow monitoring stations as grey circles, and the Lake Thun and Inn catchments in yellow and orange shading, respectively. Lower panels display the digital elevation model (DEM) at 250 m resolution for both catchments, while upper side panels show the corresponding aspect and slope. All coordinates are given in the Swiss CH1903+/LV95 reference system (EPSG:2056, in km).

detail for two individual catchments: the Lake Thun catchment in west-central Switzerland and the Inn catchment in the eastern Alps, highlighted in yellow and orange, respectively, in Figure 1.

The Lake Thun catchment extends roughly 50 km in both the north–south and east–west directions and covers an area of approximately 1300 km^2. The Inn catchment, by contrast, stretches about 90 km along the Engadine valley and covers approximately 2300 km^2. Elevations in both catchments range from around 500 m to more than 4000 m. The lower panels of Figure 1 show the digital elevation model (DEM) at 250 m resolution, while the upper side panels display the corresponding terrain aspect and slope of the two catchments.

https://doi.org/10.5194/egusphere-2026-2725
Preprint. Discussion started: 27 May 2026

2.2 FSM2OSHD snow model

FSM2OSHD (Mott et al., 2023) is a fully distributed, physics-based snow model of intermediate complexity, solving the coupled mass and energy balance for individual numerical snow layers without explicitly accounting for snow microstructure and metamorphism. FSM2OSHD is based on the Flexible Snow Model (FSM Essery, 2015; Essery et al., 2025) and has been specifically adapted, extended, and tuned for use within the Swiss Operational Snow Hydrological Service (OSHD Mott et al., 2023). In this study, the model is forced with hourly data from the numerical weather prediction (NWP) model ICON (Zängl et al., 2015), run by the Swiss Federal Office for Meteorology and Climatology (MeteoSwiss). The 1 km resolution NWP data are downscaled using dedicated statistical and dynamical downscaling schemes to the 250 m model resolution (Mott et al., 2023).

The assimilation of SCF observations presented hereafter (Section 2.5) is based on an ensemble simulation created by perturbing two terrain-dependent model parameters that control the grid-cell specific albedo decay and precipitation input. Local changes to the albedo decay scheme affect the seasonal ripening of the snowpack, while slope-dependent adjustments to the precipitation input affect the representation of snow redistribution patterns, together accounting for small-scale errors in accumulation and ablation patterns. The following sections briefly outline the surface albedo parameterization, the precipitation multiplier, and the SCF parameterization. For further details on model implementation, please refer to Mott et al. (2023); Essery (2015); Essery et al. (2025).

2.2.1 Albedo parametrization

The albedo parametrization in FSM2OSHD follows Douville et al. (1995) and Essery et al. (2013) with specific operational adaptations and tuning (Mott et al., 2023; Cluzet et al., 2024). The broadband snow surface albedo α is a prognostic variable that decays from its maximum fresh-snow value $\alpha_{\text{fresh}}^{\text{max}} = 0.86$ as a function of time. The albedo decay for each time step follows a linear decay rate for cold snow and an exponential decay rate for melting snow, determined based on the snow surface temperature T_{surf}.

$$\Delta\alpha_{\text{decay}} = \begin{cases} -\frac{\Delta t}{\tau_{\text{cold}}} & \text{for} \quad T_{\text{surf}} < 0\,^{\circ}\text{C} \\ (\alpha - \alpha_{\text{min}}) \left(\exp\left(-\frac{\Delta t}{\tau_{\text{melt}}} \right) - 1 \right) & \text{for} \quad T_{\text{surf}} \geq 0\,^{\circ}\text{C} \end{cases} \tag{1}$$

The decay time scales for cold and melting snow are $\tau_{\text{cold}} = 3000\,\text{h}$ and $\tau_{\text{melt}} = 130\,\text{h}$, respectively, and the minimum albedo of melting snow is set to $\alpha_{\text{min}} = 0.6$.

To account for the gradual brightening of the snow surface during snowfall, the albedo increases proportionally to the amount of snowfall (SF) in that time step. If the 24 h accumulation of snow $SF_{24\text{h}}$ exceeds the threshold $SF_{\text{min}} = 10\,\text{mm}$, the surface albedo value fully resets to its maximum value $\alpha_{\text{fresh}}^{\text{max}}$.

$$\alpha = \begin{cases} \alpha_{\text{fresh}}^{\text{max}} & \text{if} \quad SF_{24\text{h}} > SF_{\text{min}}, \\ \alpha + (\alpha_{\text{fresh}}^{\text{max}} - \alpha) \frac{SF}{SF_{\text{min}}} & \text{otherwise.} \end{cases} \tag{2}$$

https://doi.org/10.5194/egusphere-2026-2725
Preprint. Discussion started: 27 May 2026

Additionally, the parametrization accounts for vegetation and soil shining through thin snowpacks with a total SWE below 75 mm by reducing $\alpha_{\text{fresh}}^{\text{max}}$ by 20 %.

The initial tuning of the minimum, maximum, and threshold parameters is based on flat-field snow depth and SWE observations (Mott, 2023) and was recently refined using wet-snow maps derived from Sentinel-1 retrievals (Cluzet et al., 2024). In addition, an aspect-dependency was introduced to mitigate a delay in the modeled melt onset, identified especially on southerly slopes relative to Sentinel-1 wet-snow observations (Cluzet et al., 2024). The dynamical downscaling routine for shortwave radiation estimates incoming radiation for each grid cell separately for horizontal and inclined surfaces, explicitly resolving local slopes and shading from the surrounding terrain (Jonas et al., 2020). The ratio of inclined radiation to horizontal radiation is then used to scale the albedo decay timescales, τ. The same ratio is also employed in the definition of the albedo-change perturbations, as described in Section 2.5.1.

2.2.2 Precipitation multiplier

Mountain snow cover is characterized by strong spatial heterogeneity due to preferential deposition over complex terrain and wind- and gravity-driven redistribution processes (Mott et al., 2018). Explicitly resolving such processes in snow models requires simulations at hectometer or finer spatial resolutions and corresponding accurate wind forcing (Quéno et al., 2024; Berg et al., 2024; Reynolds et al., 2024). At coarser spatial resolutions, FSM2OSHD parameterizes these terrain effects by applying an empirical slope-dependent precipitation multiplier (e.g., Blöschl et al., 1991; Huss et al., 2008), which reduces the amount of solid precipitation over steep terrain to better reproduce observed accumulation patterns. The precipitation multiplier pm is computed via a hyperbolic tangent function of the slope angle β (in degrees), calibrated against high-resolution distributed snow depth observations based on airborne photogrammetry data (Vögeli et al., 2016).

$$pm(\beta) = p_1 \ \tanh\left(p_2 \ (\beta - p_3)\right) \ + \ (1 - p_1) \tag{3}$$

The parameters $p_1 = 0.32$, $p_2 = -4.3$, and $p_3 = 37\,^\circ$ are fitted to match distributed snow depth observation from airborne Lidar scans across the European Alps (Grünewald and Lehning, 2015). The precipitation multiplier is computed for a 25 m resolution DEM and then upscaled to account for subgrid variability within the 250 m model grid cells.

2.2.3 Snow cover fraction parametrization

The SCF parametrization of FSM2OSHD tracks the seasonal evolution of snow depth and SWE to account for alternating accumulation and ablation patterns dependent on the topographic subgrid variability (Helbig et al., 2021b). The subgrid parametrization is based on an empirical relationship between mean snow depths d and its standard deviation σ_d estimated from detailed distributed snow depths observations at the peak of winter (Helbig et al., 2015). For each time step, three separate SCF estimates are computed to account for both seasonal evolution and short-term changes, as detailed below. The maximum of the three values determines the final SCF estimate.

https://doi.org/10.5194/egusphere-2026-2725
Preprint. Discussion started: 27 May 2026

The algorithm computes the seasonal SCF using a hyperbolic tangent function as

$$SCF = \tanh(1.3\frac{d}{\sigma_d}). \tag{4}$$

Here σ_d depends on the snow depths and the topographic subgrid variabilities in slope and elevations obtained from a high-resolution DEM (Helbig et al., 2015), with further adjustments to account for scale-dependent effects (Helbig et al., 2021a). Furthermore, the algorithm uses the most recent minimum snow depth as a value for d, and the current seasonal maximum snow depth to compute σ_d (Helbig et al., 2021b).

To account for abrupt increases in SCF following snowfall events, two additional SCF values are computed, the first based on the snow accumulated over the previous 14 days and the second based on the most recent snowfall event (Helbig et al., 2021b). To ensure that only the new snow contributes to these values, as if it had fallen on bare ground, the SCF is calculated using the same formulation as in Eq. 4, but with the change in snow depth Δd rather than the absolute value. Under the assumption that new snow is deposited relatively homogeneously across the grid cell, σ_d depends solely on Δd following a simple power law (Egli and Jonas, 2009), disregarding any potential subgrid variability.

2.3 Particle Filter and Particle Batch Smoother

The particle filter (PF, Chopin and Papaspiliopoulos, 2020) is a Bayesian data assimilation method that represents the true but unknown state of a system by sequentially updating a set of weighted ensemble members, the so-called particles. The prior distribution, which reflects the model uncertainty, is estimated from an ensemble simulation, typically generated by perturbing input data, model parameters, and/or model states. As observations become available, particle weights are updated based on the agreement between simulated and observed values. This is done via the likelihood function, which reflects the probability of observing the given value under the assumption that the particle represents the true state of the system. The resulting posterior distribution combines the prior estimate with the observational information, accounting for their respective uncertainties, yielding a more precise and more accurate estimate. To mitigate the risk of filter degeneracy, in which only a few particles retain non-negligible weights, a resampling step is commonly applied. Thereby, low-weight particles are discarded, while high-weight particles are duplicated, after which the weights are reset. The (resampled) particles of the posterior are then propagated forward in time by the model dynamics, forming the prior for the next assimilation cycle, in which the weighting step is repeated with new observations. Through this iterative process and the absence of any Gaussian assumption, the PF is particularly well suited to nowcasting frameworks that employ complex, nonlinear models.

The Particle Batch Smoother (PBS, Margulis et al., 2015) can be viewed as a PF that assimilates all available observations within a given time period, rather than sequentially assimilating individual observations as they become available. Analogous to the filter, the PBS operates on a set of weighted ensemble members, whereby the weights reflect the integrated evidence from all observations over the respective periods. Hence, the PBS computes the particles' weights based on their trajectories over the entire assimilation window, rather than their final state at the end of the assimilation window. Because of this retrospective nature, PBS and other ensemble smoothers are commonly used in reanalysis applications (e.g., Aalstad et al., 2018).

https://doi.org/10.5194/egusphere-2026-2725
Preprint. Discussion started: 27 May 2026

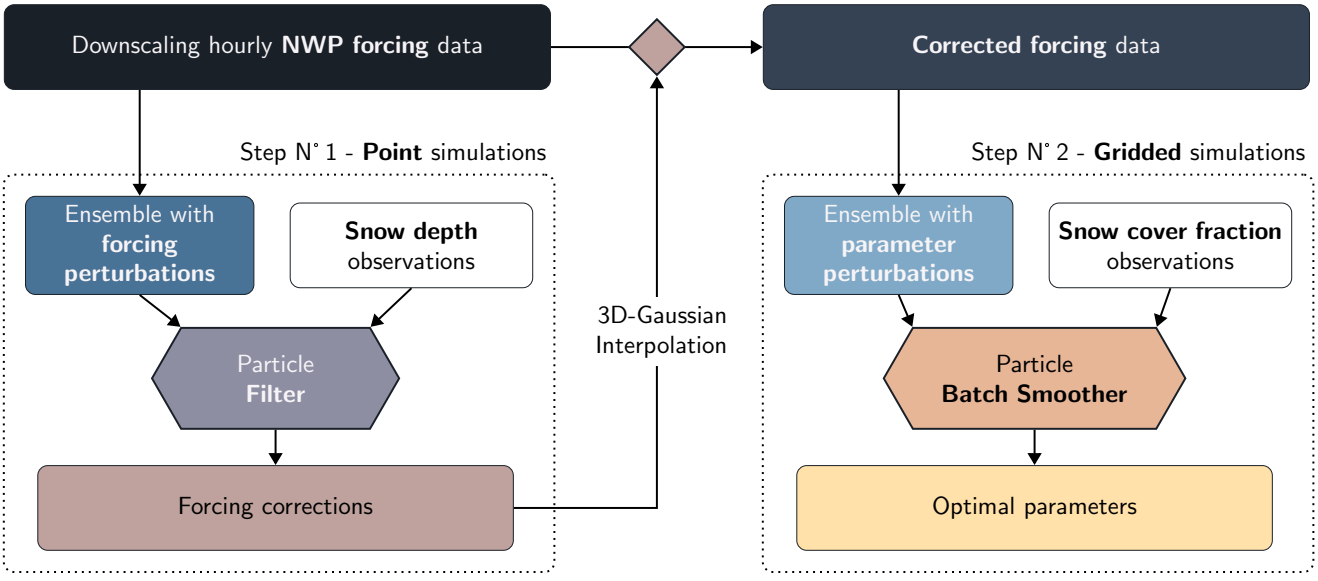

Figure 2. Simplified workflow of the two-step assimilation scheme.

2.4 Step 1: PF-based assimilation of in situ snow depth observations

This first assimilation step targets subregional error patterns in the meteorological forcing by assimilating snow depth observations from 444 snow monitoring stations over sequential three-day windows, following Oberrauch et al. (2024). This section briefly summarizes the approach. An in-depth description of the method, along with a comprehensive validation and sensitivity analysis, is provided in Oberrauch et al. (2024) and Oberrauch et al. (2025).

The PF-based assimilation scheme relies on ensemble simulations at all station locations, generated by perturbing incoming longwave radiation, air temperature, and precipitation. Additive perturbations of incoming longwave radiation and air temperature are sampled from the central 80 % of normal distributions with mean $\mu_{\mathrm{LW}} = \mu_{\mathrm{TA}} = 0$, and standard deviations $\sigma_{\mathrm{LW}} = 117\,\mathrm{W/m^2}$ and $\sigma_{\mathrm{TA}} = 2.73\,^{\circ}\mathrm{C}$, respectively. The precipitation input is scaled using factors drawn from the central 80 % of a log-normal distribution with parameters $\mu_{\mathrm{PR}} = 0$ and $\sigma_{\mathrm{PR}} = 1.174$. This perturbation strategy modifies the radiative energy input and the amount and phase of precipitation (the latter via temperature-based phase partitioning), resulting in an ensemble of modeled snow depths that typically encompasses the observations (Oberrauch et al., 2025).

The agreement between simulated and observed snow depths is evaluated sequentially at the end of each three-day assimilation window to update particle weights. Specifically, the weight of each particle ω_i^t is determined from the mismatch between simulated $d_{\mathrm{sim},i}^t$ and observed snow depths d_{obs}^t:

$$\omega_i^t \propto \exp\left(-0.5\left(\frac{d_{\mathrm{sim},i}^t - d_{\mathrm{obs}}^t}{\sigma_{\mathrm{obs}}^t}\right)^2\right). \tag{5}$$

https://doi.org/10.5194/egusphere-2026-2725
Preprint. Discussion started: 27 May 2026

Here, σ^t_{obs} denotes the observation uncertainty, set to 5 % of the observed snow depth, with lower and upper bounds of 5 and 20 cm, respectively (following Oberrauch et al., 2025). The weights are normalized such that $\sum_i \omega^t_i = 1$.

Rather than retaining the full posterior distribution and propagating it into the next assimilation window, the probabilistic information is deliberately collapsed by selecting the mode of the perturbation posterior, i.e., the point of highest probability density. In cases of equifinality, where multiple local modes share comparably high probability density, we select the most conservative solution, namely the one closest to the unperturbed state (Oberrauch et al., 2024, Section 2.3). This yields a single set of optimal forcing corrections for each station and assimilation window, which are subsequently interpolated to unobserved locations across the domain following Oberrauch et al. (2024, Section 2.4). For each model grid cell, a three-dimensional Gaussian interpolation (Jörg-Hess et al., 2014) estimates the forcing corrections from all stations within a 35 km radius, weighted by the combined horizontal and vertical distance between station and grid cell (whereby the vertical distance is scaled by a factor $\gamma = 50$). These correction fields are then applied to the downscaled forcing data that drive the gridded simulations in the second assimilation step (see the workflow diagram in Figure 2).

2.5 Step 2: PBS-based assimilation of SCF observations

After correcting the dominant uncertainties in the forcing data at subregional scales, SCF observations can be used to address the remaining seasonally stationary, cumulative errors in small-scale accumulation and ablation patterns. Individually, SCF observations provide only limited information about the instantaneous model state for most of the season, as they primarily capture the onset of snow cover and the timing of melt-out (Jiang and Shi, 2026). However, the temporal evolution of snow cover derived from multiple SCF observations enables the reconstruction of snowpack dynamics over the entire season (e.g., Girotto et al., 2014b; Margulis et al., 2015). The novelty of this study lies in incorporating such temporally sparse yet spatially distributed information into an operational nowcasting framework.

As illustrated in Figure 2, the second assimilation step builds on the corrected forcing data and aims to adjust key model parameters by assimilating spatially distributed SCF observations using a PBS. Following Oberrauch et al. (2024), each observed grid cell is treated independently during the assimilation, after which the probabilistic information is collapsed onto a single set of optimal model parameters that are subsequently interpolated across the domain.

The assimilation scheme is based on an ensemble of simulations generated by perturbing the albedo decay and the precipitation multiplier, allowing for grid-cell-specific adjustments to melt and accumulation processes. Modifying the broadband snow albedo by accelerating or decelerating its decay directly affects the energy balance and, consequently, the seasonal ripening of the snowpack. Adjusting the precipitation multiplier function, in turn, enables a better representation of snow redistribution patterns. To maintain computational efficiency, the ensemble comprises 36 members, resulting from the factorial combination of six albedo decay perturbations and six precipitation multiplier perturbations (see Section 2.5.1). The perturbations are defined such that their effects depend on the aspect and slope angle of each grid cell, while flat grid cells remain unperturbed (see Figure 3). This design ensures that the forcing corrections inferred from flat-field station locations in the first assimilation step remain applicable, thereby enabling a consistent combination of both steps.

https://doi.org/10.5194/egusphere-2026-2725
Preprint. Discussion started: 27 May 2026

The results presented hereafter are based on the PBS assimilation of all available SCF observations from January to June, intended to showcase the full potential of the approach by the end of the ablation season. Accordingly, each ensemble member is assigned a single weight ω_i that represents the integrated evidence from all observations.

$$\omega_i \propto \exp\left(-0.5\ \Sigma_{t=1}^{N_t}\left(\frac{SCF_{\text{obs}}^t - SCF_{\text{sim}}^t}{\sigma_{SCF}}\right)^2\right) \tag{6}$$

Here, SCF_{obs}^t and SCF_{sim}^t refer to the observed and modeled SCF of a given grid cell at time t, respectively, N_t is the total number of observation dates, and the SCF observation uncertainty is set to $\sigma_{\text{SCF}} = 25\,\%$. A PBS is, however, equivalent to a PF without resampling (Van Leeuwen, 2012), as there is no difference between computing a single weight ω_i that accounts for all observations at once (as in Eq. 6), or sequentially updating particle weights for each observation date t and multiplying them like

$$\omega_i \propto \Pi_{t=1}^{N_t}\omega_i^t, \quad \text{with} \quad \omega_i^t = \exp\left(-0.5\ \left(\frac{SCF_{\text{obs}}^t - SCF_{\text{sim}}^t}{\sigma_{SCF}}\right)^2\right). \tag{7}$$

This equivalence implies that the presented results would be unchanged if the parameters were updated sequentially as new observations become available, which is how the method would be applied in an operational nowcasting context, as discussed in Section 4.

After the assimilation step, the optimal parameters for each observed grid cell are defined as those corresponding to the particle with the highest weight. In the case of equifinal solutions, that is, when multiple particles share the same maximum weight, the most conservative solution is selected, defined as the parameter set closest to the unperturbed values. This results in spatially distributed maps of optimal adjustments to the albedo decay and precipitation multiplier for all observed grid cells (see Figure 5a and b), which are then used for the pixel-by-pixel simulation (see Section 2.6).

The subsequent interpolation step primarily serves to propagate the inferred parameter adjustments to unobserved grid cells, such as urban, glaciated, and forested areas, as well as regions obscured by cloud cover (see Figure 5c and d). An inherent side effect of this interpolation is the smoothing of the pixel-by-pixel estimates. While the objective is to correct small-scale accumulation and ablation patterns, typically on the order of 100 m or less (Quéno et al., 2024), this smoothing may attenuate locally optimal parameter values.

2.5.1 Model parameter ensemble generation

The albedo change perturbations are based on the ratio between the incoming shortwave radiation (SW) per inclined surface SW_{incl} and the SW radiation per horizontal surface SW_{hor}. For each grid cell and each hourly time step, the albedo decay $\Delta\alpha$ is scaled by a factor 20^q, with $q(\varphi)$ defined as

$$q(\varphi) = \frac{\arctan\left(\varphi\ \log\left(\frac{SW_{\text{incl}}}{SW_{\text{hor}}}\right)\right)}{\pi/2}. \tag{8}$$

Here, $\varphi \in \{-0.58, 0, 0.2, 0.58, 1.71, 5\}$ is the varying perturbation parameter that scales for the arcus tangens function. The arcus tangens function is normalized by $\pi/2$ so that the resulting range of q lies between $[-1, 1]$. The resulting scaling factor

https://doi.org/10.5194/egusphere-2026-2725
Preprint. Discussion started: 27 May 2026

of the hourly albedo change for different values of φ is shown in the left panel of Figure 3, covering a (theoretical) range of $20^q \in [0.05, 20]$. Edge cases where either SW_{incl}, SW_{hor}, or both are zero are handled by setting q to -1, 1, or 0, respectively.

The perturbations of the precipitation multiplier change the p_3 parameter in Equation (3), which defines the inflection point of the tangens hyperbolicus (i.e., the slope angle where the curvature changes). Proper scaling ensures that the precipitation multiplier for flat grid cells equals $pm = 1$ while retaining its original minimum value of $pm = 0.36$. Hence, for a given slope angle β and a given perturbation ζ, the perturbed precipitation multiplier pm' is defined as

$$pm'(\beta,\zeta) = 0.36 + (1 - 0.36)\ \frac{\vartheta(\beta,\zeta) - \vartheta(90\,°,\zeta)}{\vartheta(0\,°,\zeta) - \vartheta(90\,°,\zeta)}, \tag{9}$$

where

$$\vartheta(\beta,\zeta) = \tanh(p_2\ (\beta - \zeta)), \quad \text{with} \quad p_2 = -4.3. \tag{10}$$

In other words, lower (higher) values of ζ shift the inflection point towards flatter (steeper) slopes, resulting in a reduced (increased) amount of solid precipitation.

For $\zeta = z = 37\,°$, the perturbed precipitation multiplier reduces back to the original Equation (3). In addition to this zero-member, we chose the following perturbation values $\zeta \in \{10, 20, 30, 37, 40, 50, 60\}$. The right panel of Figure 3 illustrates the perturbed precipitation multiplier functions for the selected values of ζ.

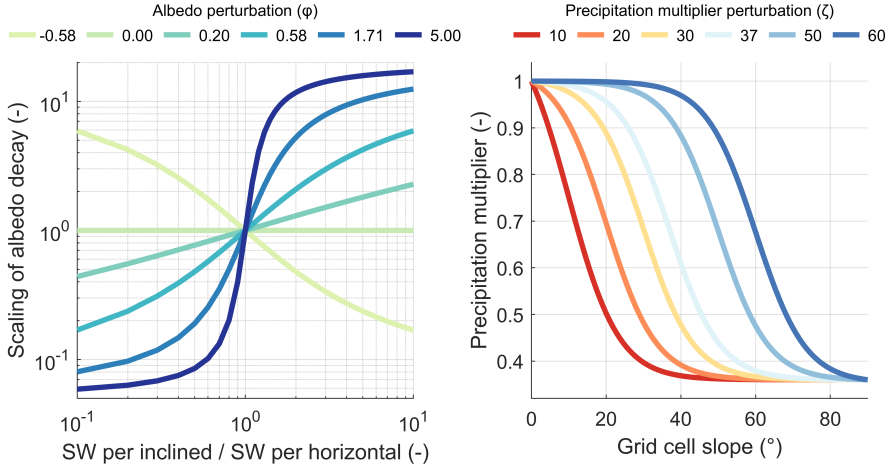

Figure 3. Model parameter perturbations used in the second assimilation step. The left panel shows the scaling of hourly albedo decay as a function of the ratio between incoming shortwave radiation on the inclined surface (SW_{incl}) and on a horizontal surface (SW_{hor}) for different perturbation values φ. The right panel shows the precipitation multiplier as a function of slope angle for different perturbation values ζ. Here, the albedo perturbation $\varphi = 0.00$ and the precipitation multiplier perturbation $\zeta = 37\,°$ represent the original, unperturbed formulations.

https://doi.org/10.5194/egusphere-2026-2725
Preprint. Discussion started: 27 May 2026

2.5.2 Multidimensional Gaussian interpolation of model parameter adjustments

In analogy to Oberrauch et al. (2024), we use a multidimensional Gaussian interpolation scheme adapted from Jörg-Hess et al. (2014). For each target grid cell (denote by a), the interpolated parameters are computed as a weighted average of the 49 nearest source cells (denoted by b), with weights determined by a Gaussian scaling of the n-dimensional distance as $\omega_{\mathrm{a,b}} \propto \exp\left(-0.5\, r_{\mathrm{a,b}}/\sigma_{\mathrm{interp}}\right)$. The n-dimensional distance $r_{\mathrm{a,b}}$ is computed from the horizontal distance in x- and y-direction, $\Delta x_{\mathrm{a,b}}$ and $\Delta y_{\mathrm{a,b}}$, and a scaled difference of the aspect predictor Ψ for the albedo change parameter

$$r_{\mathrm{a,b}}^{\mathrm{albedo}} = \sqrt{(\Delta x_{\mathrm{a,b}})^2 + (\Delta y_{\mathrm{a,b}})^2 + (\gamma_\psi\, \Delta\Psi_{\mathrm{a,b}})^2}, \tag{11}$$

or a scaled difference in slope angle β for the precipitation multiplier

$$r_{\mathrm{a,b}}^{\mathrm{prec.mult.}} = \sqrt{(\Delta x_{\mathrm{a,b}})^2 + (\Delta y_{\mathrm{a,b}})^2 + (\gamma_\beta\, \Delta\beta_{\mathrm{a,b}})^2}. \tag{12}$$

Based on the sensitivity analysis presented in Section 3.4, the interpolation parameters are define as $\sigma_{\mathrm{interp}} = 250\,\mathrm{m}$ and $\gamma_\psi = \gamma_\beta \equiv \gamma = 250\,\mathrm{m}/5\,^\circ$.

The aspect predictor is computed from the cosine of the aspect angle ψ shifted by $-45\,^\circ$, which appropriately accounts for the circular nature of aspect angles. The shift reflects the assumption that differences in aspects have unequal influence across sectors. Differences in the south-east and north-west sectors are assumed to have a greater impact due to the lower solar angles during morning and evening hours. In contrast, the same variations in the north-east and south-west sectors, which receive minimal and maximal solar input, respectively, are assumed to have a comparatively smaller effect. Hence, the aspect predictor is computed as

$$\Delta\Psi_{\mathrm{a,b}} = 90\,^\circ \cdot \left(\cos(\psi_{\mathrm{a}} - 45\,^\circ) - \cos(\psi_{\mathrm{b}} - 45\,^\circ)\right). \tag{13}$$

Therein, to allow for a valid scaling with γ in Equation 11, the difference of the cosine functions is multipled by $90\,^\circ$, yielding a range of $\Psi \in [\pm 90\,^\circ]$.

2.5.3 SCF assimilation data

We assimilate spaceborne SCF maps based on Sentinel-2 retrievals provided by the AlpSnow science activity within the European Space Agency's Alpine Regional Initiative (European Space Agency, 2025). The AlpSnow SCF product is generated by applying multi-spectral unmixing to Level-1C reflectance data, which improves snow detection in shaded terrain by exploiting spectral differences across the available spectral reflective bands (Keuris et al., 2023). The product is provided at 0.0002 ° pixel spacing in a latitude-longitude grid on the WGS84 ellipsoid (EPSG:4326), corresponding to approximately 20 m in the Swiss CH1903+/LV95 reference system (EPSG:2056) used by the model.

Known limitations of spaceborne optical snow cover observations include difficulties in differentiating between snow, bare ice (on glaciers), and clouds (especially thin cirrus), identifying cloud shadows, and accurately detecting snow cover within forests (Keuris et al., 2023; Barrou Dumont et al., 2021). To mitigate these issues, SCF retrievals are masked for clouds, glaciers,

https://doi.org/10.5194/egusphere-2026-2725
Preprint. Discussion started: 27 May 2026

forests, and urban areas at the 10 m subpixel level before aggregation to the 250 m model resolution. The classification of each model grid cell follows a weighted voting scheme adapted from Cluzet et al. (2024). A grid cell is masked as cloud, forest, or urban area when more than 50 %, 66 %, or 33 % of its subpixels correspond to the respective class. This reflects a lenient forest threshold to preserve snow information in partially forested areas and a stricter one for urban areas. Glacier and water body masks are directly applied within FSM2OSHD (Mott et al., 2023). All landcover information is based on the CORINE dataset (European Union's Copernicus Land Monitoring Service information, 2020), with the forest classification being refined using additional high-resolution canopy data (Webster et al., 2025). The final SCF value for non-masked 250 m grid cells is computed as the mean over all valid, non-masked subpixels. Additionally, we manually discard observations on dates where most of the domain is cloud-covered and only a few scattered grid cells are observed.

2.6 Experimental design for evaluating the second assimilation step

To evaluate the second assimilation step, we present four distinct simulations, all forced with the same corrected meteorological input data derived from PF-based assimilation of in situ snow depth observations (as outlined in Section 2.4).

1. The control simulation without any adjustment to the albedo decay or precipitation multiplier.
2. The pixel-by-pixel simulation applies the best model parameters estimated independently for each of the observed grid cells, as outlined above. For grid cells without any valid SCF observations (i.e., forested, glaciated, urban, or cloud-covered grid cells), no parameter adjustments can be computed, and these unobserved grid cells will run with the original configuration identical to the control run.
3. To update the simulation at all grid cells, including those without direct observations, we run a simulation that interpolates the parameters from the observed grid cells using an N-dimensional Gaussian interpolation scheme as defined in Section 2.5.2. While interpolation smooths the pixel-by-pixel parameters, we can still only validate the simulation at observed grid cells, which are not fully independent in this setup.
4. We also run a simulation using a leave-one-*pixel*-out (LOO) interpolation of the estimated parameters, which serves as a proxy for fully independent validation. Therefore, we interpolate the optimal model parameters for each grid cell from the surrounding cells, disregarding the values estimated at the respective target cell.

3 Results

3.1 Two-step assimilation scheme

To provide a qualitative illustration of the proposed two-step assimilation framework, Figure 4 compares the progressive improvements in modeled snow-cover patterns for the Inn catchment as the two assimilation steps are applied. To this end, the simulated SCF maps are compared against Sentinel-2 observations acquired on June 19, 2024. Panel (a) shows the reference

https://doi.org/10.5194/egusphere-2026-2725
Preprint. Discussion started: 27 May 2026

simulation without assimilation, which substantially overestimates the extent of snow cover, as reflected by the large dark blue areas in the corresponding difference map shown in panel (b).

The first assimilation step, in which forcing corrections inferred from in situ snow depth observations are applied, leads to markedly improved agreement with the observed SCF, as shown in panel (c). Accordingly, the corresponding difference map (panel d) exhibits smaller deviations that are more closely centered around zero. This demonstrates that the information contained in in situ snow depth observations is sufficient to correct forcing errors at the subregional scale, whereas errors associated with small-scale accumulation and ablation patterns that deviate from flat-field conditions remain unresolved (c.f. Oberrauch et al., 2025).

The second assimilation step addresses these remaining errors by adjusting model parameters that control the snowpack evolution in sloped terrain relative to the flat-field station locations. Assimilating SCF observations to optimize parameters controlling local albedo decay and snow redistribution (panel e) almost completely removes the differences between the simulated and observed SCF (panel f). It shows that the dominant uncertainties in the forcing data can be reduced through the first assimilation step, while the second step effectively targets the remaining small-scale errors in snowpack evolution. Since the PF-based assimilation framework used in the first step is described and validated in detail by Oberrauch et al. (2024, 2025), the following sections focus on the second step of assimilating SCF observations.

3.2 Parameter estimation and interpolation

Figure 5 presents the estimated optimal adjustments to the albedo decay parametrization and the precipitation multiplier for the Lake Thun catchment over the winter season 2022/23. Panels (a) and (b) show the pixel-by-pixel estimates, available only where observations are available, while panels (c) and (d) display the interpolated and smoothed parameter fields covering the entire domain. Because the assimilation scheme targets local corrections at the slope scale, the resulting parameter fields exhibit substantial pixel-to-pixel variability, and the patterns reflect multiple terrain characteristics, including slope and aspect, beyond simple spatial proximity.

A first qualitative interpretation suggests that the optimal albedo change parameters (Figure 5a) are generally higher along ridge lines and lower in valley bottoms, however, with considerable spatial heterogeneity. In contrast, the precipitation multiplier exhibits (Figure 5b) slightly more coherent spatial patterns, generally aligned along the mountain range's northern and southern sides. These distinct spatial patterns indicate that adjustments to the albedo decay and the precipitation multiplier provide sufficiently independent handles on the evolution of the snowpack. Furthermore, a statistical assessment indicates that global correlations between the perturbation parameters and various topographic characteristics, such as aspect, slope, and elevation, are weak (results not shown). This aligns with the goal of correcting only non-systematic, small-scale errors in accumulation and ablation patterns that a global, terrain-dependent tuning cannot resolve.

The interpolation estimates the model parameters for unobserved locations by drawing from grid cells in the immediate neighborhood and on the same or adjacent aspects and hill slopes. The resulting parameter maps (Figure 5c and d) therefore exhibit complex spatial structures that reflect multiple topographic dimensions. Note that interpolation produces continuous parameter fields rather than the discrete perturbation parameters shown in pixel-by-pixel estimation. For improved compara-

https://doi.org/10.5194/egusphere-2026-2725
Preprint. Discussion started: 27 May 2026

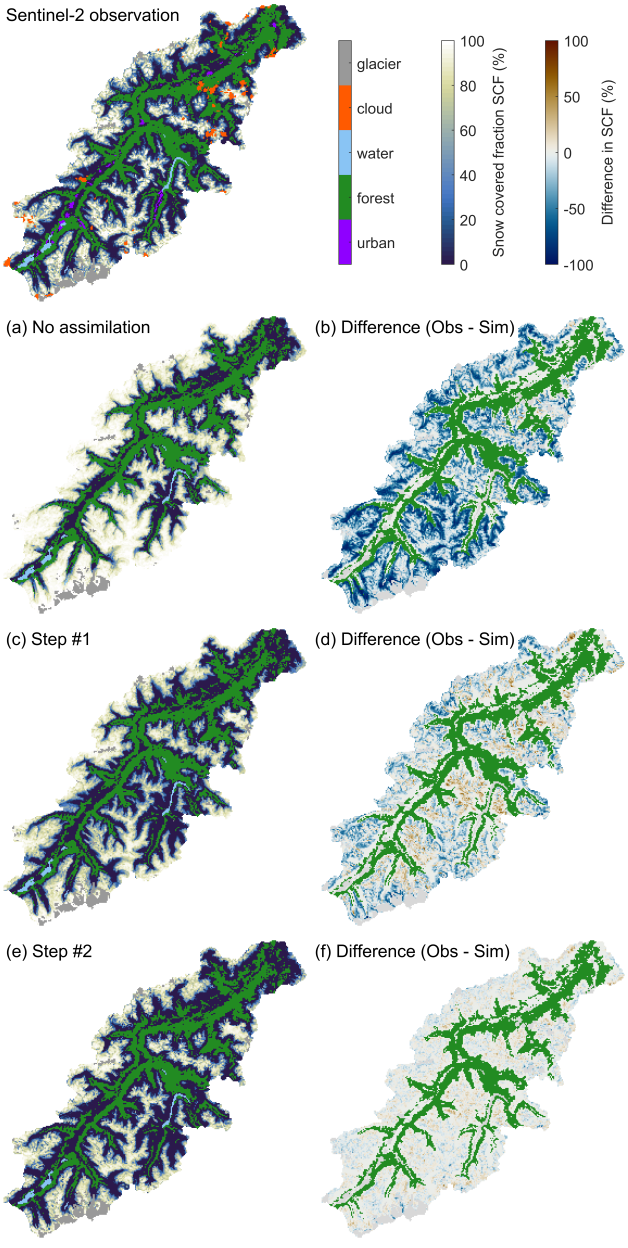

Figure 4. Observed and modeled snow-cover fraction maps for the Inn catchment on June 19, 2024. Sentinel-2-based observations are shown in the upper-left panel. Panel (a) shows the reference simulation without assimilation, panel (c) the simulation after applying the forcing corrections inferred in the first assimilation step, and panel (e) the simulation after additionally optimizing model parameters in the second assimilation step. The corresponding difference maps are shown in the right-hand panels (b), (d), and (f), respectively.

https://doi.org/10.5194/egusphere-2026-2725
Preprint. Discussion started: 27 May 2026

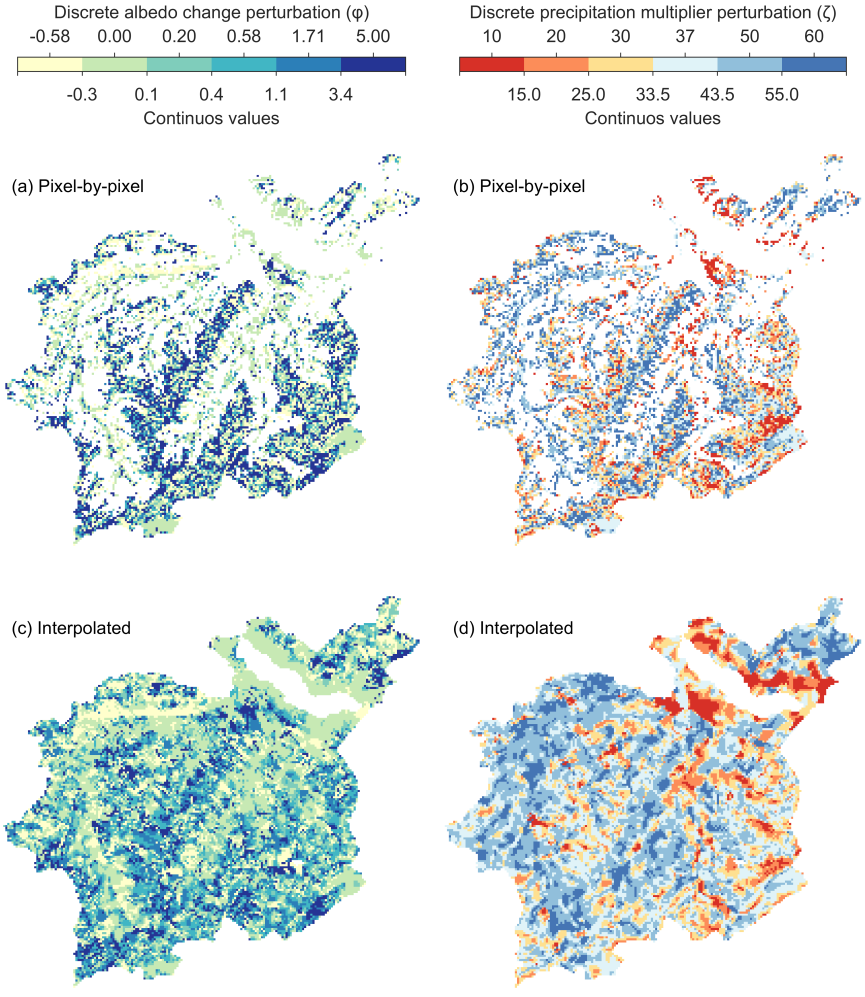

Figure 5. Parameter adjustments to the albedo decay and the precipitation multiplier inferred from the SCF assimilation. The upper panels show pixel-by-pixel estimates, whereas the lower panels show interpolated parameters. Note that in the upper panels, the unobserved grid cells shown in white, where no parameter updates are computed, use the default parameters ($\varphi = 0$ and $\zeta = 37$).

https://doi.org/10.5194/egusphere-2026-2725
Preprint. Discussion started: 27 May 2026

bility, particularly of the nonlinear albedo parameters, the lower panels also show discretized values, with class boundaries placed at the midpoints between the initial perturbation levels. Since the resulting patterns depend on the parameters of the Gaussian interpolation scheme (as defined in Section 2.5.2), a dedicated sensitivity analysis to these parameters is presented in Section 3.4.

3.3 Improvements in SCF estimates

Figure 6 shows SCF observations and model bias of the different simulations for the Lake Thun catchment on May 4, 2023. The control simulation, shown in panel (a), generally overestimates SCF relative to the observations, shown in the top-left panel, except that it underestimates SCF on southwesterly slopes near the observed snow line altitude. The pixel-by-pixel simulation with adjusted parameters, shown in panel (d), provides a substantially better match to the observations and reduces both over- and underestimation apparent in the control run. Nonetheless, some biases remain, mostly positive on the westerly to northerly slopes, visible along the ridge line in the center, and in the foothills of the high mountains to the south of the catchment. Expectedly, the same bias patterns are even more pronounced in both the interpolated and the leave-one-out runs, in panels (b) and (c), respectively, even though both still outperform or match the performance of the control simulation. It should be noted, however, that this assessment on May 4 is not necessarily representative of the model's performance over the entire season.

Figure 7 shows the temporal evolution of SCF RMSE and bias between January and July 2023, with the observational coverage of the catchment for each retrieval date shown in the uppermost panel. The pixel-by-pixel simulation yields lower RMSE and absolute bias than the control simulation throughout most of the season, reducing the RMSE by about 50 % from May onward. The interpolated simulation yields RMSE and bias values between those of the control and pixel-by-pixel simulations, corresponding to a reduction in RMSE of about 25 %. While improvements in the LOO simulations are expected to be the lowest, they still show a decrease in RMSE of about 10 % relative to the control run. These improvements are largely constrained to the late ablation season, while the performance earlier in the season is, as expected, comparable to that of the control simulation. The bias of all shown experiments is comparatively small, with absolute values below 15 % and mostly even below 10 %. As with the RMSE, improvements in bias are most notable during the ablation season and are strongest for the pixel-by-pixel simulation, with less improvement for the interpolated and LOO simulations.

Overall, the performance differences between the simulations are most pronounced during the ablation season, starting in April 2023, again because SCF observations are most influential in this data assimilation context during periods of partial snow cover. Hence, for observations taken shortly after snowfall events (e.g., in mid-March), the differences between simulations diminish, largely because the fresh-snow SCF parameterization is only weakly sensitive to adjustments to albedo decay and the precipitation multiplier, and SCF values increase to 100% over most of the domain. On the contrary, snow-free conditions over large parts of the domain in the late season tend to reduce RMSE and bias across all simulations. Nevertheless, a seasonal bias pattern remains evident, with negative bias (underestimation of SCF) during the accumulation season until mid-March and positive bias (overestimation) during the ablation period.

Figure 8 shows RMSE and bias for January to July 2023, but for the entire model domain. As in the Lake Thun catchment (Figure 7), the pixel-by-pixel simulation clearly outperforms the control run throughout the season. Notably, the interpolated

https://doi.org/10.5194/egusphere-2026-2725
Preprint. Discussion started: 27 May 2026

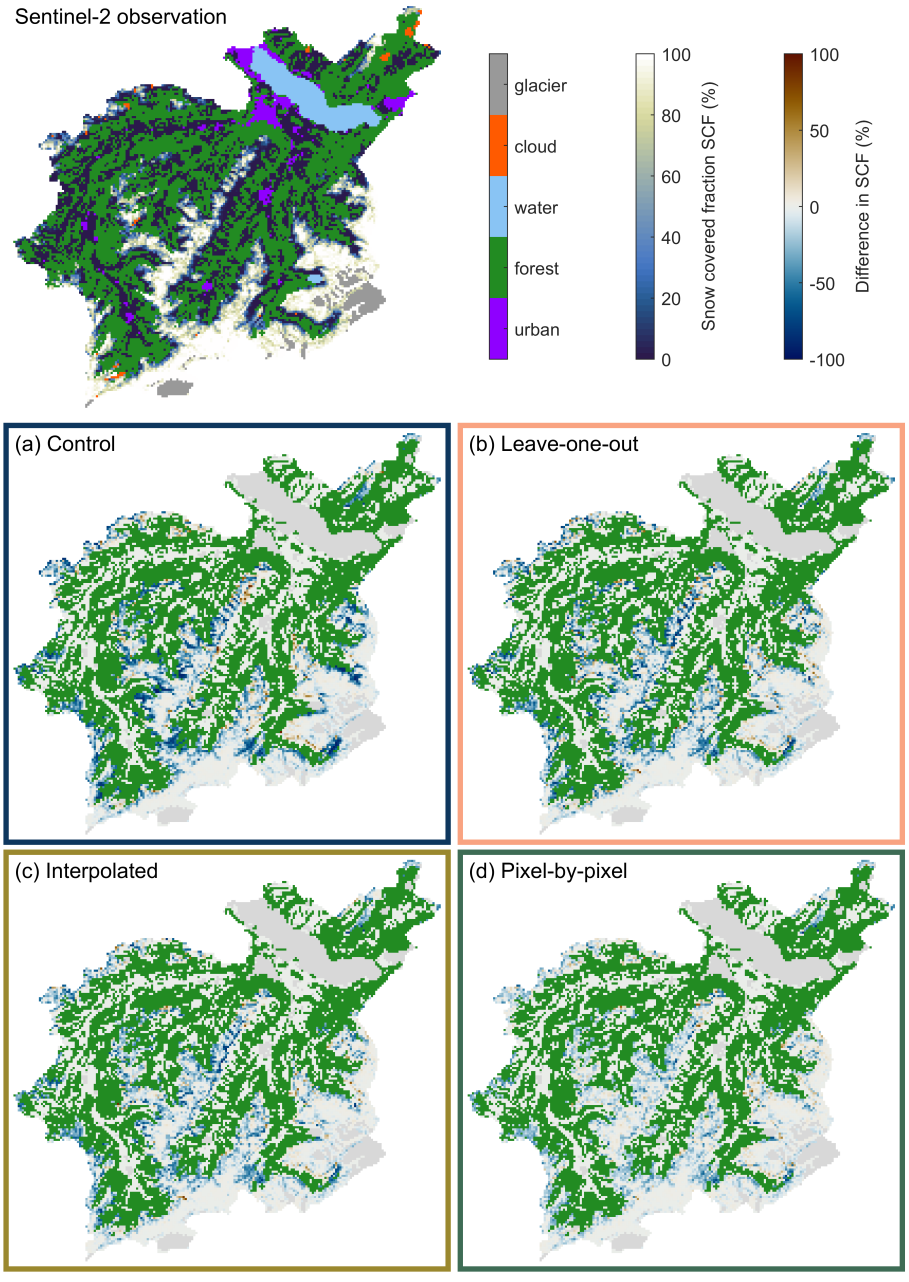

Figure 6. Snow cover fraction observations and model bias (Obs. - Sim.) for Lake Thun catchment on May 4, 2023. The postprocessed observation based on Sentinel-2 retrievals is shown in the top-left panel. The model SCF biases of the control, leave-one-out, interpolated, and pixel-by-pixel simulations are shown in panels (a), (b), (c), and (d), respectively, with forested areas in green. Note that the forest masks for the observation and the simulations are not identical.

https://doi.org/10.5194/egusphere-2026-2725
Preprint. Discussion started: 27 May 2026

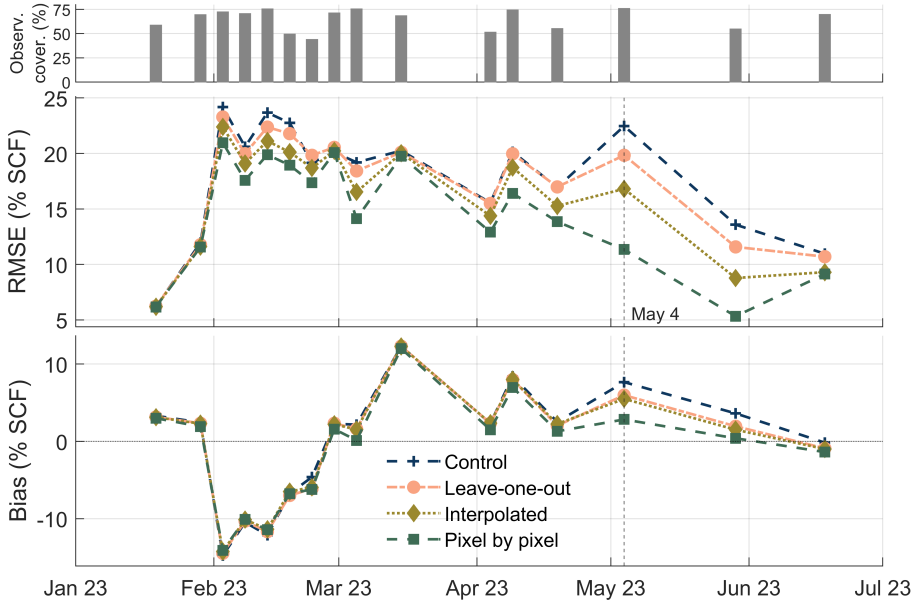

Figure 7. RMSE (central panel) and bias (lower panel) between January and June 2023, across the different experiments. The upper panel indicates the observational coverage, i.e., the percentage of observed grid cells in the corresponding SCF map. The vertical dashed line indicates May 4, 2023, which is shown in Figures 6.

and LOO runs also show consistent improvements throughout the season, indicating arguably better domain-wide performance than for the Lake Thun catchment alone. The observed improvements are therefore not limited to a single catchment but are representative of the broader model domain, suggesting that the insights gained from the following sensitivity experiment in the Lake Thun catchment are generalizable for the full domain.

3.4 Sensitivity to the interpolation parameters

Although the assimilated SCF observations are, in principle, fully spatially distributed, limitations of optical retrievals require that information be propagated to unobserved grid points. The multidimensional Gaussian interpolation scheme used for this purpose has two key parameters (see Section 2.5.2). The standard deviation σ defines how the trust in neighboring information is scaled with distance, while the scaling factor γ modulates the relative importance of horizontal distance versus differences in aspect and slope for the albedo change parameter and the precipitation multiplier.

Figure 9 illustrates the interpolated precipitation multiplier fields for four parameter combinations. As expected, a wider standard deviation (larger σ values) and a stronger weighting of horizontal distance over slope angle differences (larger γ values) yield smoother spatial patterns. Thereby, variations in σ have a stronger impact than changes in γ, indicating that the radius of influence exerts greater control over the interpolation than the relative weighting of horizontal distance and terrain differences. The leave-one-out interpolation fields are not shown, as they are visually almost indistinguishable from the standard

https://doi.org/10.5194/egusphere-2026-2725
Preprint. Discussion started: 27 May 2026

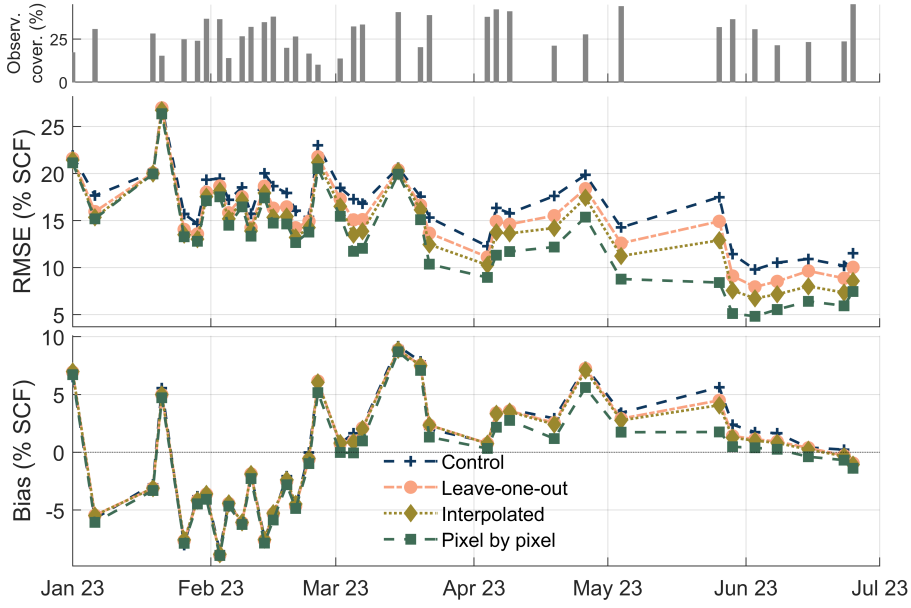

Figure 8. Sames as Figure 7, but for the entire model domain.

interpolation results, despite having a considerable influence on simulation outcomes (compare RMSE of the interpolated and leave-one-out simulations in Figure 7).

Figure 10 shows RMSE values between January and July 2023 (same as Figure 7) for six combinations of interpolation parameters, with $\sigma \in \{250, 400, 800\,\mathrm{m}\}$ and $250\,\mathrm{m} \equiv \gamma \in \{5, 10, 15\,^\circ\}$. The upper panel shows the RMSE of interpolated simulations, while the lower panel shows the RMSE of the leave-one-out simulation. As expected, a more local interpolation (smaller σ and γ values) results in better performance of the interpolated simulations, because the interpolated parameter fields remain closer to the pixel-by-pixel estimates. Thus, sensitivity to differences in aspect and slope decreases with wider standard deviations; in simulations with $\sigma = 800\,\mathrm{m}$, the values of γ appear to have no effect.

The leave-one-out simulations exhibit minimal sensitivity to the interpolation parameters. Interestingly, stronger local interpolation does not lead to overfitting or degraded performance. Instead, simulations using smaller σ values perform slightly better overall, while variations in γ have a negligible impact. Based on this assessment, we chose $\sigma = 250\,\mathrm{m}$ and $\gamma = \frac{250\,\mathrm{m}}{5^\circ}$ as interpolation parameters since they perform best in both the interpolated and leave-one-out simulations.

4 Discussion

This study demonstrates improvements in distributed snowpack estimates by applying stationary updates to selected model parameters inferred from a PBS assimilation of multiple SCF observations within a single season. The most obvious strategy for operational implementation within a nowcasting framework is to update the PBS-based parameters whenever new SCF observations with sufficient coverage become available. Such sequential assimilation without resampling would progressively

https://doi.org/10.5194/egusphere-2026-2725
Preprint. Discussion started: 27 May 2026

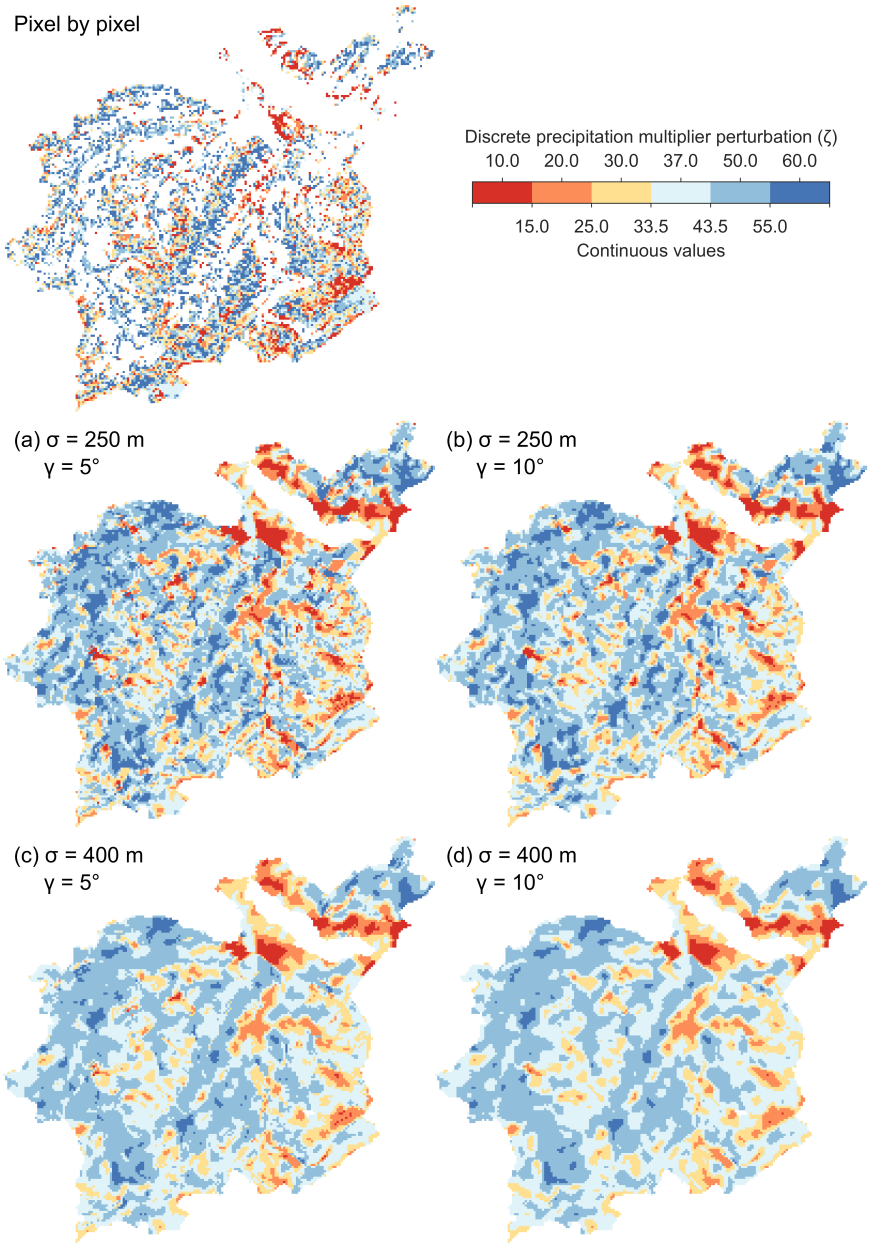

Figure 9. Results of the interpolated adjustments to the precipitation multiplier for different values of the interpolation parameters (σ and γ), based on the pixel-by-pixel estimates shown in the uppermost panel (wherein unobserved grid cells are shown in white).

https://doi.org/10.5194/egusphere-2026-2725
Preprint. Discussion started: 27 May 2026

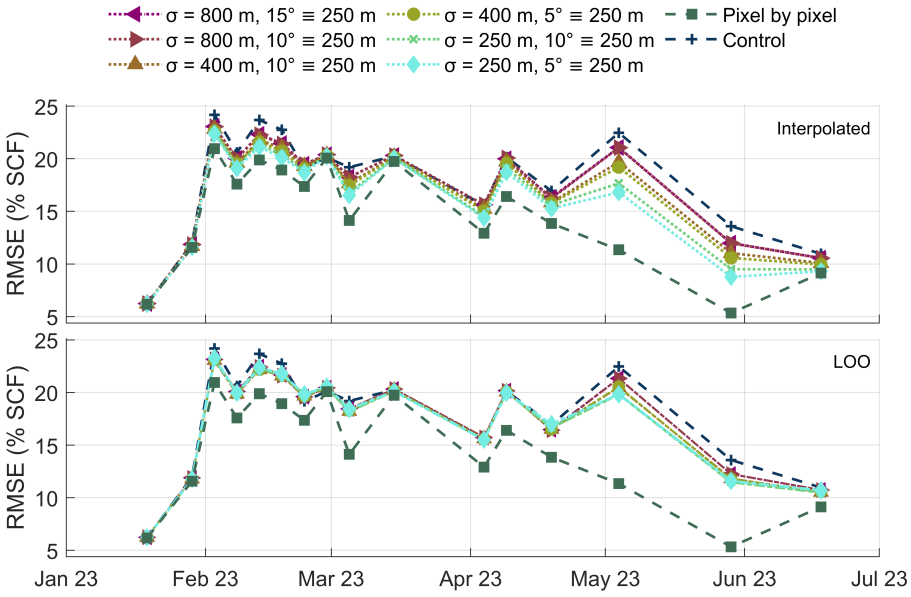

Figure 10. RMSE of the different sensitivity experiments with varying interpolation parameters between January and June 2023, with the interpolation simulations in the upper panel and the leave-one-out simulations in the lower panel.

refine parameter estimates over the course of the season at minimal additional computational cost, requiring only repeated assimilation and interpolation steps, with no additional ensemble simulations. The deterministic simulation using the interpolated parameters would need to be restarted from the beginning of the season after each update, but given its deterministic nature, this remains computationally feasible. Based on the results presented in Section 3.3, however, major improvements in the model estimates are not expected until the beginning of the ablation season, when the SCF observations become increasingly informative. Nevertheless, since the operational model domain spans from near sea level to 4500 m, regions of partial snow cover can be found somewhere across the domain throughout most of the winter, suggesting that improvements to the model estimates can be expected at any given time, albeit not uniformly across the entire domain.

An alternative strategy would be to estimate optimal parameters for multiple distinct seasonal phases, e.g., accumulation, ripening, and ablation, through sequential PBS assimilation, with a reset or resampling step between phases. However, this approach faces a fundamental limitation of SCF observations as, at any given location, both observed and modeled SCF values remain close to 100 % for most of the local snow season, resulting in near-identical particle weights across ensemble members. This is already evident in the RMSE and bias time series (Figures 7 and 8), which show little sensitivity to different parameters during the accumulation season. Consequently, all perturbations would be assigned nearly equal likelihood, and, in our setup, the most conservative, non-perturbed member would be selected as optimal, which in turn undermines the rationale for having multiple assimilation windows in the first place. More fundamentally, local adjustments to both the albedo decay and precipitation multiplier are most effective when applied consistently over a substantial portion of the season, as model short-

https://doi.org/10.5194/egusphere-2026-2725
Preprint. Discussion started: 27 May 2026

comings may have accumulated for months before SCF observations become informative. Constraining parameter adjustments to the depletion period would therefore likely require unrealistically large perturbations to compensate for errors that have accumulated throughout the season.

A key question for any distributed snow data assimilation scheme concerns spatial correlation and the extent to which improvements at observed locations can inform unobserved locations. The leave-one-out simulations show only marginal improvement over the control simulations, suggesting that SCF-derived adjustments to the albedo decay and the precipitation multiplier are highly local and cannot be easily propagated to neighboring unobserved cells. Other patterns of spatial correlation across topographic dimensions not tested in this study, such as terrain position indices or climatological meltout timing, may nevertheless exist and should be explored in future work, following the example of Alonso-González et al. (2023); Mazzolini et al. (2025). Despite limited performance gains at unobserved locations, the improvements at observed grid cells are substantial. From an operational perspective, it would be inappropriate to disregard this information simply because unobserved locations do not benefit to the same extent. The leave-one-out results further indicate that applying interpolated parameters across the domain does not degrade model performance at unobserved locations, although performance within forests could not be evaluated.

While we are directly comparing observed and modeled SCF, the retrieval of SCF data from spaceborne spectral reflectance data, as well as the model's internal SCF parameterization, are additional sources of uncertainty. The assimilated SCF data are not direct observations but are derived from reflectance data through multi-spectral unmixing (Keuris et al., 2023), followed by masking of clouds, forests, and urban areas, and upscaling to the model resolution (Cluzet et al., 2024). Each of these post-processing steps contributes to the uncertainty of the assimilated data. On the other hand, SCF is not a physical state within FSM2OSHD but rather computed through a complex subgrid parametrization based on snow depth, SWE, and snowfall history (Helbig et al., 2021b). Hence, the comparison between modeled and observed SCF may be intrinsically flawed, despite the assimilation scheme already accounting for the relevant uncertainties. For example, the model's fresh-snow SCF parameterization (as outlined in Section 2.2.3) assigns an SCF of 97 % for a snow depth of only 15 cm, which might be realistic for flat meadows but not for rugged mountain terrain. On the other hand, shallow snowpacks viewed from space may appear less bright, corresponding to an observed SCF of less than 100 %, particularly when vegetation or soil is visible beneath the snow (Keuris et al., 2023; Cluzet et al., 2024). This mismatch highlights an additional source of structural uncertainty that could be mitigated by adapting the model's SCF parametrization.

5 Conclusions

This study demonstrates the potential of combined assimilation of in situ snow depth observations and spaceborne SCF observations in an operational snow-modeling application. The proposed framework follows a two-step approach, driven by the availability of assimilation data and operational constraints on computational efficiency. First, subregional errors in the meteorological forcing are corrected by assimilating flat-field in situ snow depth observations (following Oberrauch et al., 2024). Second, two key model parameters controlling small-scale accumulation and ablation processes are adjusted via a PBS as-

https://doi.org/10.5194/egusphere-2026-2725
Preprint. Discussion started: 27 May 2026

simulation of spatially distributed SCF observations derived from Sentinel-2 data. An important design feature ensures that model parameters at flat locations remain unaffected, allowing the two assimilation steps to be independent from each other. Grid-cell-specific adjustments to the aspect-dependent albedo decay and the slope-dependent precipitation multiplier improve the representation of melt timing, melt rates, and preferential deposition and redistribution patterns, which are otherwise underresolved by the model physics. The parameter adjustments are distributed across the domain to unobserved grid cells using a local interpolation scheme based on the horizontal distance and differences in aspect and slope. While substantial improvements are achieved at observed grid cells, unobserved grid cells, evaluated using a leave-one-out strategy, benefit to a lesser extent.

Because SCF observations contain the most useful information primarily during periods of partial snow cover, the chosen PBS approach enables estimation of stationary parameter adjustments that best reconstruct the seasonal evolution of the snowpack. For an operational nowcasting application, however, sequential updates of the PBS without resampling could progressively refine parameter estimates over the season, with updates performed whenever valid SCF observations become available. In this context, the potential benefit of partitioning the season into multiple assimilation windows should also be investigated.

Code and data availability. The source code of the FSM2OSHD snow model is publicly accessible at https://github.com/oshd-slf/FSM2oshd. Meteorological forcing data can be obtained from MeteoSwiss under https://www.meteoswiss.admin.ch/services-and-publications/service/open-data.html. In situ snow depth measurements from the monitoring network are provided by the WSL Institute for Snow and Avalanche Research SLF at https://measurement-data.slf.ch/ and by MeteoSwiss at https://data.geo.admin.ch/browser/index.html#/collections/ch.meteoschweiz.ogd-nime. Snow cover fraction maps derived from Sentinel-2 imagery are distributed through ESA's AlpSnow EXPRO+ project at https://alpsnow.enveo.at/.

Competing interests. The authors declare no conflict of interest.

Acknowledgements. This work was partially funded by the Swiss National Science Foundation under grant 192140 (https://data.snf.ch/grants/grant/192140), within the project "Improved methods for incorporating observational data into physics-based, multi-layer snow models". Language refinement and text editing were supported by generative AI tools.

https://doi.org/10.5194/egusphere-2026-2725
Preprint. Discussion started: 27 May 2026

References

Aalstad, K., Westermann, S., Schuler, T. V., Boike, J., and Bertino, L.: Ensemble-based assimilation of fractional snow-covered area satellite retrievals to estimate the snow distribution at Arctic sites, Cryosphere, 12, 247–270, https://doi.org/10.5194/TC-12-247-2018, 2018.

Alonso-González, E., Gutmann, E., Aalstad, K., Fayad, A., Bouchet, M., and Gascoin, S.: Snowpack dynamics in the Lebanese mountains from quasi-dynamically downscaled ERA5 reanalysis updated by assimilating remotely sensed fractional snow-covered area, Hydrol. Earth Syst. Sci, 25, 4455–4471, https://doi.org/10.5194/hess-25-4455-2021, 2021.

Alonso-González, E., Aalstad, K., Baba, M. W., Revuelto, J., López-Moreno, J. I., Fiddes, J., Essery, R., and Gascoin, S.: The Multiple Snow Data Assimilation System (MuSA v1.0), Geoscientific Model Development, 15, 9127–9155, https://doi.org/10.5194/gmd-15-9127-2022, 2022.

Alonso-González, E., Aalstad, K., Pirk, N., Mazzolini, M., Treichler, D., Leclercq, P., Westermann, S., López-Moreno, J. I., and Gascoin, S.: Spatio-temporal information propagation using sparse observations in hyper-resolution ensemble-based snow data assimilation, Hydrol. Earth Syst. Sci, 27, 4637–4659, https://doi.org/10.5194/hess-27-4637-2023, 2023.

Baba, M., Gascoin, S., and Hanich, L.: Assimilation of Sentinel-2 Data into a Snowpack Model in the High Atlas of Morocco, Remote Sensing, 10, 1982, https://doi.org/10.3390/rs10121982, 2018.

Barnett, T. P., Adam, J. C., and Lettenmaier, D. P.: Potential impacts of a warming climate on water availability in snow-dominated regions, Nature, 438, 303–309, https://doi.org/10.1038/nature04141, 2005.

Barrou Dumont, Z., Gascoin, S., Hagolle, O., Ablain, M., Jugier, R., Salgues, G., Marti, F., Dupuis, A., Dumont, M., and Morin, S.: Brief communication: Evaluation of the snow cover detection in the Copernicus High Resolution Snow & Ice Monitoring Service, Cryosphere, 15, 4975–4980, https://doi.org/10.5194/TC-15-4975-2021, 2021.

Beniston, M., Farinotti, D., Stoffel, M., Andreassen, L. M., Coppola, E., Eckert, N., Fantini, A., Giacona, F., Hauck, C., Huss, M., Huwald, H., Lehning, M., López-Moreno, J.-I., Magnusson, J., Marty, C., Morán-Tejéda, E., Morin, S., Naaim, M., Provenzale, A., Rabatel, A., Six, D., Stötter, J., Strasser, U., Terzago, S., and Vincent, C.: The European mountain cryosphere: a review of its current state, trends, and future challenges, The Cryosphere, 12, 759–794, https://doi.org/10.5194/tc-12-759-2018, 2018.

Berg, J., Reynolds, D., Quéno, L., Jonas, T., Lehning, M., and Mott, R.: A seasonal snowpack model forced with dynamically downscaled forcing data resolves hydrologically relevant accumulation patterns, Frontiers in Earth Science, 12, 1393 260, https://doi.org/10.3389/feart.2024.1393260, 2024.

Blöschl, G.: Scaling issues in snow hydrology, Hydrological Processes, 13, 2149–2175, https://doi.org/10.1002/(SICI)1099-1085(199910)13:14/15<2149::AID-HYP847>3.0.CO;2-8, 1999.

Blöschl, G., Kirnbauer, R., and Gutknecht, D.: Distributed Snowmelt Simulations in an Alpine Catchment: 1. Model Evaluation on the Basis of Snow Cover Patterns, Water Resources Research, 27, 3171–3179, https://doi.org/10.1029/91WR02250, 1991.

Bühler, Y., Marty, M., Egli, L., Veitinger, J., Jonas, T., Thee, P., and Ginzler, C.: Snow depth mapping in high-alpine catchments using digital photogrammetry, Cryosphere, 9, 229–243, https://doi.org/10.5194/TC-9-229-2015, 2015.

Bührle, L. J., Marty, M., Eberhard, L. A., Stoffel, A., Hafner, E. D., and Bühler, Y.: Spatially continuous snow depth mapping by aeroplane photogrammetry for annual peak of winter from 2017 to 2021 in open areas, The Cryosphere, 17, 3383–3408, https://doi.org/10.5194/tc-17-3383-2023, 2023.

Cantet, P., Boucher, M. A., Lachance-Coutier, S., Turcotte, R., and Fortin, V.: Using a particle filter to estimate the spatial distribution of the snowpack water equivalent, Journal of Hydrometeorology, 20, 577–594, https://doi.org/10.1175/JHM-D-18-0140.1, 2019.

https://doi.org/10.5194/egusphere-2026-2725
Preprint. Discussion started: 27 May 2026

Carrassi, A., Bocquet, M., Bertino, L., and Evensen, G.: Data assimilation in the geosciences: An overview of methods, issues, and perspectives, WIREs Climate Change, 9, https://doi.org/10.1002/wcc.535, 2018.

Charrois, L., Cosme, E., Dumont, M., Lafaysse, M., Morin, S., Libois, Q., and Picard, G.: On the assimilation of optical reflectances and snow depth observations into a detailed snowpack model, Cryosphere, 10, 1021–1038, https://doi.org/10.5194/TC-10-1021-2016, 2016.

Chopin, N. and Papaspiliopoulos, O.: An Introduction to Sequential Monte Carlo, vol. 4 of *Springer Series in Statistics*, Springer International Publishing, Cham, https://doi.org/10.1007/978-3-030-47845-2, 2020.

Clark, M. P., Hendrikx, J., Slater, A. G., Kavetski, D., Anderson, B., Cullen, N. J., Kerr, T., Örn Hreinsson, E., and Woods, R. A.: Representing spatial variability of snow water equivalent in hydrologic and land-surface models: A review, Water Resources Research, 47, https://doi.org/10.1029/2011WR010745, 2011.

Cluzet, B., Revuelto, J., Lafaysse, M., Tuzet, F., Cosme, E., Picard, G., Arnaud, L., and Dumont, M.: Towards the assimilation of satellite reflectance into semi-distributed ensemble snowpack simulations, Cold Regions Science and Technology, 170, https://doi.org/10.1016/J.COLDREGIONS.2019.102918, 2020.

Cluzet, B., Lafaysse, M., Deschamps-Berger, C., Vernay, M., and Dumont, M.: Propagating information from snow observations with CrocO ensemble data assimilation system: a 10-years case study over a snow depth observation network, The Cryosphere, 16, 1281–1298, https://doi.org/10.5194/tc-16-1281-2022, 2022.

Cluzet, B., Magnusson, J., Quéno, L., Mazzotti, G., Mott, R., and Jonas, T.: Exploring how Sentinel-1 wet-snow maps can inform fully distributed physically based snowpack models, The Cryosphere, 18, 5753–5767, https://doi.org/10.5194/tc-18-5753-2024, 2024.

De Lannoy, G. J. M., Bechtold, M., Albergel, C., Brocca, L., Calvet, J.-C., Carrassi, A., Crow, W. T., de Rosnay, P., Durand, M., Forman, B., Geppert, G., Girotto, M., Hendricks Franssen, H.-J., Jonas, T., Kumar, S., Lievens, H., Lu, Y., Massari, C., Pauwels, V. R. N., Reichle, R. H., and Steele-Dunne, S.: Perspective on satellite-based land data assimilation to estimate water cycle components in an era of advanced data availability and model sophistication, Frontiers in Water, 4, https://doi.org/10.3389/frwa.2022.981745, 2022.

Deschamps-Berger, C., Cluzet, B., Dumont, M., Lafaysse, M., Berthier, E., Fanise, P., and Gascoin, S.: Improving the Spatial Distribution of Snow Cover Simulations by Assimilation of Satellite Stereoscopic Imagery, Water Resources Research, 58, https://doi.org/10.1029/2021WR030271, 2022.

DeWalle, D. R. and Rango, A.: Principles of Snow Hydrology, Cambridge University Press, https://doi.org/10.1017/CBO9780511535673, 2008.

Douville, H., Royer, J. F., and Mahfouf, J. F.: A new snow parameterization for the Météo-France climate model: Part I: validation in stand-alone experiments, Climate Dynamics, 12, 21–35, https://doi.org/10.1007/BF00208760, 1995.

Dozier, J., Bair, E. H., and Davis, R. E.: Estimating the spatial distribution of snow water equivalent in the world's mountains, WIREs Water, 3, 461–474, https://doi.org/10.1002/wat2.1140, 2016.

Eckert, N., Corona, C., Giacona, F., Gaume, J., Mayer, S., van Herwijnen, A., Hagenmuller, P., and Stoffel, M.: Climate change impacts on snow avalanche activity and related risks, Nature Reviews Earth & Environment, 5, 369–389, https://doi.org/10.1038/s43017-024-00540-2, 2024.

Egli, L. and Jonas, T.: Hysteretic dynamics of seasonal snow depth distribution in the Swiss Alps, Geophysical Research Letters, 36, https://doi.org/10.1029/2008GL035545, 2009.

Essery, R.: A factorial snowpack model (FSM 1.0), Geoscientific Model Development, 8, 3867–3876, https://doi.org/10.5194/gmd-8-3867-2015, 2015.

https://doi.org/10.5194/egusphere-2026-2725
Preprint. Discussion started: 27 May 2026

Essery, R., Morin, S., Lejeune, Y., and B Ménard, C.: A comparison of 1701 snow models using observations from an alpine site, Advances in Water Resources, 55, 131–148, https://doi.org/10.1016/J.ADVWATRES.2012.07.013, 2013.

Essery, R., Mazzotti, G., Barr, S., Jonas, T., Quaife, T., and Rutter, N.: A Flexible Snow Model (FSM 2.1.1) including a forest canopy, Geoscientific Model Development, 18, 3583–3605, https://doi.org/10.5194/gmd-18-3583-2025, 2025.

European Space Agency: ESA EXPRO+ AlpSnow, https://alpsnow.enveo.at/index.html, 2025.

European Union's Copernicus Land Monitoring Service information: CORINE Land Cover 2018 (vector/raster 100 m), Europe, 6-yearly, https://doi.org/10.2909/960998c1-1870-4e82-8051-6485205ebbac, 2020.

Fiddes, J., Aalstad, K., and Westermann, S.: Hyper-resolution ensemble-based snow reanalysis in mountain regions using clustering, Hydrology and Earth System Sciences, 23, 4717–4736, https://doi.org/10.5194/HESS-23-4717-2019, 2019.

Gascoin, S., Grizonnet, M., Bouchet, M., Salgues, G., and Hagolle, O.: Theia Snow collection: High-resolution operational snow cover maps from Sentinel-2 and Landsat-8 data, Earth System Science Data, 11, 493–514, https://doi.org/10.5194/ESSD-11-493-2019, 2019.

Gascoin, S., Luojus, K., Nagler, T., Lievens, H., Masiokas, M., Jonas, T., Zheng, Z., and De Rosnay, P.: Remote sensing of mountain snow from space: status and recommendations, Frontiers in Earth Science, 12, 1381 323, https://doi.org/10.3389/feart.2024.1381323, 2024.

Girotto, M., Cortés, G., Margulis, S. A., and Durand, M.: Examining spatial and temporal variability in snow water equivalent using a 27 year reanalysis: Kern River watershed, Sierra Nevada, Water Resources Research, 50, 6713–6734, https://doi.org/10.1002/2014WR015346, 2014a.

Girotto, M., Margulis, S. A., and Durand, M.: Probabilistic SWE reanalysis as a generalization of deterministic SWE reconstruction techniques, Hydrological Processes, 28, 3875–3895, https://doi.org/10.1002/hyp.9887, 2014b.

Girotto, M., Musselman, K. N., and Essery, R. L. H.: Data Assimilation Improves Estimates of Climate-Sensitive Seasonal Snow, Current Climate Change Reports, 6, 81–94, https://doi.org/10.1007/s40641-020-00159-7, 2020.

Girotto, M., Formetta, G., Azimi, S., Bachand, C., Cowherd, M., De Lannoy, G., Lievens, H., Modanesi, S., Raleigh, M. S., Rigon, R., and Massari, C.: Identifying snowfall elevation patterns by assimilating satellite-based snow depth retrievals, Science of The Total Environment, 906, 167 312, https://doi.org/10.1016/J.SCITOTENV.2023.167312, 2024.

Grünewald, T. and Lehning, M.: Are flat-field snow depth measurements representative? A comparison of selected index sites with areal snow depth measurements at the small catchment scale, Hydrological Processes, 29, 1717–1728, https://doi.org/10.1002/HYP.10295, 2015.

Grünewald, T., Schirmer, M., Mott, R., and Lehning, M.: Spatial and temporal variability of snow depth and ablation rates in a small mountain catchment, The Cryosphere, 4, 215–225, https://doi.org/10.5194/TC-4-215-2010, 2010.

Günther, D., Marke, T., Essery, R., and Strasser, U.: Uncertainties in Snowpack Simulations—Assessing the Impact of Model Structure, Parameter Choice, and Forcing Data Error on Point-Scale Energy Balance Snow Model Performance, Water Resources Research, 55, 2779–2800, https://doi.org/10.1029/2018WR023403, 2019.

Günther, D., Hanzer, F., Warscher, M., Essery, R., and Strasser, U.: Including Parameter Uncertainty in an Intercomparison of Physically-Based Snow Models, Frontiers in Earth Science, 8, 498, https://doi.org/10.3389/feart.2020.542599, 2020.

Helbig, N., van Herwijnen, A., Magnusson, J., and Jonas, T.: Fractional snow-covered area parameterization over complex topography, Hydrology and Earth System Sciences, 19, 1339–1351, https://doi.org/10.5194/hess-19-1339-2015, 2015.

Helbig, N., Bühler, Y., Eberhard, L., Deschamps-Berger, C., Gascoin, S., Dumont, M., Revuelto, J., S. Deems, J., and Jonas, T.: Fractional snow-covered area: Scale-independent peak of winter parameterization, Cryosphere, 15, 615–632, https://doi.org/10.5194/TC-15-615-2021, 2021a.

https://doi.org/10.5194/egusphere-2026-2725
Preprint. Discussion started: 27 May 2026

Helbig, N., Schirmer, M., Magnusson, J., Mäder, F., van Herwijnen, A., Quéno, L., Bühler, Y., Deems, J. S., and Gascoin, S.: A seasonal algorithm of the snow-covered area fraction for mountainous terrain, The Cryosphere, 15, 4607–4624, https://doi.org/10.5194/tc-15-4607-2021, 2021b.

Helmert, J., Şorman, A. , Montero, R. A., De Michele, C., de Rosnay, P., Dumont, M., Finger, D. C., Lange, M., Picard, G., Potopová, V., Pullen, S., Vikhamar-Schuler, D., and Arslan, A. N.: Review of Snow Data Assimilation Methods for Hydrological, Land Surface, Meteorological and Climate Models: Results from a COST HarmoSnow Survey, Geosciences 2018, Vol. 8, Page 489, 8, 489, https://doi.org/10.3390/GEOSCIENCES8120489, 2018.

Hock, R., Rasul, G., Adler, C., Cáceres, B., Gruber, S., Hirabayashi, Y., Jackson, M., Kääb, A., Kang, S., Kutuzov, S., Milner, A., Molau, U., Morin, S., Orlove, B., and Steltzer, H. I.: High Mountain Areas, in: The Ocean and Cryosphere in a Changing Climate, edited by Pörtner, H.-O., Roberts, D., Masson-Delmotte, V., P. Zhai, M. T., Poloczanska, E., Mintenbeck, K., Alegría, A., Nicolai, M., Okem, A., Petzold, J., Rama, B., and Weyer, N., chap. 2, pp. 131–202, Cambridge University Press, https://doi.org/10.1017/9781009157964.004, 2022.

Huss, M., Bauder, A., Funk, M., and Hock, R.: Determination of the seasonal mass balance of four Alpine glaciers since 1865, Journal of Geophysical Research: Earth Surface, 113, https://doi.org/10.1029/2007JF000803, 2008.

Immerzeel, W. W., Lutz, A. F., Andrade, M., Bahl, A., Biemans, H., Bolch, T., Hyde, S., Brumby, S., Davies, B. J., Elmore, A. C., Emmer, A., Feng, M., Fernández, A., Haritashya, U., Kargel, J. S., Koppes, M., Kraaijenbrink, P. D. A., Kulkarni, A. V., Mayewski, P. A., Nepal, S., Pacheco, P., Painter, T. H., Pellicciotti, F., Rajaram, H., Rupper, S., Sinisalo, A., Shrestha, A. B., Viviroli, D., Wada, Y., Xiao, C., Yao, T., and Baillie, J. E. M.: Importance and vulnerability of the world's water towers, Nature, 577, 364–369, https://doi.org/10.1038/s41586-019-1822-y, 2020.

Jiang, L. and Shi, J.: Snow Cover Mapping, Comprehensive Remote Sensing, pp. 237–259, https://doi.org/10.1016/B978-0-443-13220-9.00024-X, 2026.

Jonas, T., Webster, C., Mazzotti, G., and Malle, J.: HPEval: A canopy shortwave radiation transmission model using high-resolution hemispherical images, Agricultural and Forest Meteorology, 284, 107 903, https://doi.org/10.1016/J.AGRFORMET.2020.107903, 2020.

Jörg-Hess, S., Fundel, F., Jonas, T., and Zappa, M.: The Cryosphere Homogenisation of a gridded snow water equivalent climatology for Alpine terrain: methodology and applications, The Cryosphere, 8, 471–485, https://doi.org/10.5194/tc-8-471-2014, 2014.

Keuris, L., Hetzenecker, M., Nagler, T., Mölg, N., and Schwaizer, G.: An Adaptive Method for the Estimation of Snow-Covered Fraction with Error Propagation for Applications from Local to Global Scales, Remote Sensing 2023, Vol. 15, Page 1231, 15, 1231, https://doi.org/10.3390/RS15051231, 2023.

Largeron, C., Dumont, M., Morin, S., Boone, A., Lafaysse, M., Metref, S., Cosme, E., Jonas, T., Winstral, A., and Margulis, S. A.: Toward Snow Cover Estimation in Mountainous Areas Using Modern Data Assimilation Methods: A Review, Frontiers in Earth Science, 8, https://doi.org/10.3389/feart.2020.00325, 2020.

Lievens, H., Brangers, I., Marshall, H.-P., Jonas, T., Olefs, M., and De Lannoy, G.: Sentinel-1 snow depth retrieval at sub-kilometer resolution over the European Alps, The Cryosphere, 16, 159–177, https://doi.org/10.5194/tc-16-159-2022, 2022.

Liu, Y., Fang, Y., and Margulis, S. A.: Spatiotemporal distribution of seasonal snow water equivalent in High Mountain Asia from an 18-year Landsat-MODIS era snow reanalysis dataset, Cryosphere, 15, 5261–5280, https://doi.org/10.5194/TC-15-5261-2021, 2021.

López-Moreno, J. I., Fassnacht, S. R., Heath, J. T., Musselman, K. N., Revuelto, J., Latron, J., Morán-Tejeda, E., and Jonas, T.: Small scale spatial variability of snow density and depth over complex alpine terrain: Implications for estimating snow water equivalent, Advances in Water Resources, 55, 40–52, https://doi.org/10.1016/J.ADVWATRES.2012.08.010, 2013.

https://doi.org/10.5194/egusphere-2026-2725
Preprint. Discussion started: 27 May 2026

Magnusson, J., Winstral, A., Stordal, A. S., Essery, R., and Jonas, T.: Improving physically based snow simulations by assimilating snow depths using the particle filter, Water Resources Research, 53, 1125–1143, https://doi.org/10.1002/2016WR019092, 2017.

Magnusson, J., Nævdal, G., Matt, F., Burkhart, J. F., and Winstral, A.: Improving hydropower inflow forecasts by assimilating snow data, Hydrology Research, 51, 226–237, https://doi.org/10.2166/NH.2020.025, 2020.

Margulis, S. A., Girotto, M., Cortés, G., and Durand, M.: A Particle Batch Smoother Approach to Snow Water Equivalent Estimation, Journal of Hydrometeorology, 16, 1752–1772, https://doi.org/10.1175/JHM-D-14-0177.1, 2015.

Margulis, S. A., Cortés, G., Girotto, M., and Durand, M.: A Landsat-Era Sierra Nevada Snow Reanalysis (1985–2015), Journal of Hydrometeorology, 17, 1203–1221, https://doi.org/10.1175/JHM-D-15-0177.1, 2016.

Margulis, S. A., Fang, Y., Li, D., Lettenmaier, D. P., and Andreadis, K.: The Utility of Infrequent Snow Depth Images for Deriving Continuous Space-Time Estimates of Seasonal Snow Water Equivalent, Geophysical Research Letters, 46, 5331–5340, https://doi.org/10.1029/2019GL082507, 2019.

Marti, R., Gascoin, S., Berthier, E., de Pinel, M., Houet, T., and Laffly, D.: Mapping snow depth in open alpine terrain from stereo satellite imagery, The Cryosphere, 10, 1361–1380, https://doi.org/10.5194/tc-10-1361-2016, 2016.

Mazzolini, M., Aalstad, K., Alonso-González, E., Westermann, S., and Treichler, D.: Spatio-temporal snow data assimilation with the ICESat-2 laser altimeter, Cryosphere, 19, 3831–3848, https://doi.org/10.5194/TC-19-3831-2025, 2025.

Menard, C. B., Essery, R., Krinner, G., Arduini, G., Bartlett, P., Boone, A., Brutel-Vuilmet, C., Burke, E., Cuntz, M., Dai, Y., Decharme, B., Dutra, E., Fang, X., Fierz, C., Gusev, Y., Hagemann, S., Haverd, V., Kim, H., Lafaysse, M., Marke, T., Nasonova, O., Nitta, T., Niwano, M., Pomeroy, J., Schädler, G., Semenov, V. A., Smirnova, T., Strasser, U., Swenson, S., Turkov, D., Wever, N., and Yuan, H.: Scientific and Human Errors in a Snow Model Intercomparison, Bulletin of the American Meteorological Society, 102, E61–E79, https://doi.org/10.1175/BAMS-D-19-0329.1, 2021.

Morin, S., Samacoïts, R., François, H., Carmagnola, C. M., Abegg, B., Demiroglu, O. C., Pons, M., Soubeyroux, J. M., Lafaysse, M., Franklin, S., Griffiths, G., Kite, D., Hoppler, A. A., George, E., Buontempo, C., Almond, S., Dubois, G., and Cauchy, A.: Pan-European meteorological and snow indicators of climate change impact on ski tourism, Climate Services, 22, 100 215, https://doi.org/10.1016/J.CLISER.2021.100215, 2021.

Mott, R.: Seasonal snow data for Switzerland OSHD - FSM2sohd, https://doi.org/http://dx.doi.org/10.16904/envidat.404, 2023.

Mott, R., Vionnet, V., and Grünewald, T.: The Seasonal Snow Cover Dynamics: Review on Wind-Driven Coupling Processes, Frontiers in Earth Science, 6, 197, https://doi.org/10.3389/feart.2018.00197, 2018.

Mott, R., Winstral, A., Cluzet, B., Helbig, N., Magnusson, J., Mazzotti, G., Quéno, L., Schirmer, M., Webster, C., and Jonas, T.: Operational snow-hydrological modeling for Switzerland, Frontiers in Earth Science, 11, https://doi.org/10.3389/feart.2023.1228158, 2023.

Musselman, K. N., Lehner, F., Ikeda, K., Clark, M. P., Prein, A. F., Liu, C., Barlage, M., and Rasmussen, R.: Projected increases and shifts in rain-on-snow flood risk over western North America, Nature Climate Change, 8, 808–812, https://doi.org/10.1038/s41558-018-0236-4, 2018.

Oberrauch, M., Cluzet, B., Magnusson, J., and Jonas, T.: Improving Fully Distributed Snowpack Simulations by Mapping Perturbations of Meteorological Forcings Inferred From Particle Filter Assimilation of Snow Monitoring Data, Water Resources Research, 60, https://doi.org/10.1029/2023WR036994, 2024.

Oberrauch, M., Cluzet, B., Magnusson, J., and Jonas, T.: The Performance Gains of Assimilating Limited Information Into a Fully Distributed Snowpack Model Depend on Model Complexity and Input Data Quality, Water Resources Research, 61, https://doi.org/10.1029/2025WR040681, 2025.

https://doi.org/10.5194/egusphere-2026-2725
Preprint. Discussion started: 27 May 2026

Painter, T. H., Berisford, D. F., Boardman, J. W., Bormann, K. J., Deems, J. S., Gehrke, F., Hedrick, A., Joyce, M., Laidlaw, R., Marks, D., Mattmann, C., McGurk, B., Ramirez, P., Richardson, M., Skiles, S. M. K., Seidel, F. C., and Winstral, A.: The Airborne Snow Observatory: Fusion of scanning lidar, imaging spectrometer, and physically-based modeling for mapping snow water equivalent and snow albedo, Remote Sensing of Environment, 184, 139–152, https://doi.org/10.1016/j.rse.2016.06.018, 2016.

Piazzi, G., Campo, L., Gabellani, S., Castelli, F., Cremonese, E., Cella, U. M. d., Stevenin, H., and Ratto, S. M.: An Enkf-Based Scheme for Snow Multivariable Data Assimilation at an Alpine Site, Journal of Hydrology and Hydromechanics, 67, 4–19, https://doi.org/10.2478/johh-2018-0013, 2019.

Qin, Y., Abatzoglou, J. T., Siebert, S., Huning, L. S., AghaKouchak, A., Mankin, J. S., Hong, C., Tong, D., Davis, S. J., and Mueller, N. D.: Agricultural risks from changing snowmelt, Nature Climate Change 2020 10:5, 10, 459–465, https://doi.org/10.1038/s41558-020-0746-8, 2020.

Quéno, L., Mott, R., Morin, P., Cluzet, B., Mazzotti, G., and Jonas, T.: Snow redistribution in an intermediate-complexity snow hydrology modelling framework, The Cryosphere, 18, 3533–3557, https://doi.org/10.5194/tc-18-3533-2024, 2024.

Revuelto, J., Cluzet, B., Duran, N., Fructus, M., Lafaysse, M., Cosme, E., and Dumont, M.: Assimilation of surface reflectance in snow simulations: Impact on bulk snow variables, Journal of Hydrology, 603, 126 966, https://doi.org/10.1016/J.JHYDROL.2021.126966, 2021.

Reynolds, D., Quéno, L., Lehning, M., Jafari, M., Berg, J., Jonas, T., Haugeneder, M., and Mott, R.: Seasonal snow-atmosphere modeling: let's do it, The Cryosphere, 18, 4315–4333, https://doi.org/10.5194/tc-18-4315-2024, 2024.

Siirila-Woodburn, E. R., Rhoades, A. M., Hatchett, B. J., Huning, L. S., Szinai, J., Tague, C., Nico, P. S., Feldman, D. R., Jones, A. D., Collins, W. D., and Kaatz, L.: A low-to-no snow future and its impacts on water resources in the western United States, Nature Reviews Earth & Environment, 2, 800–819, https://doi.org/10.1038/s43017-021-00219-y, 2021.

Slatyer, R. A., Umbers, K. D., and Arnold, P. A.: Ecological responses to variation in seasonal snow cover, Conservation Biology, 36, e13 727, https://doi.org/10.1111/COBI.13727, 2022.

Smyth, E. J., Raleigh, M. S., and Small, E. E.: Particle Filter Data Assimilation of Monthly Snow Depth Observations Improves Estimation of Snow Density and SWE, Water Resources Research, 55, 1296–1311, https://doi.org/10.1029/2018WR023400, 2019.

Sommer, C. G., Lehning, M., and Mott, R.: Snow in a Very Steep Rock Face: Accumulation and Redistribution During and After a Snowfall Event, Frontiers in Earth Science, 3, 1–13, https://doi.org/10.3389/feart.2015.00073, 2015.

Tsang, L., Durand, M., Derksen, C., Barros, A. P., Kang, D. H., Lievens, H., Marshall, H. P., Zhu, J., Johnson, J., King, J., Lemmetyinen, J., Sandells, M., Rutter, N., Siqueira, P., Nolin, A., Osmanoglu, B., Vuyovich, C., Kim, E., Taylor, D., Merkouriadi, I., Brucker, L., Navari, M., Dumont, M., Kelly, R., Kim, R. S., Liao, T. H., Borah, F., and Xu, X.: Review article: Global monitoring of snow water equivalent using high-frequency radar remote sensing, Cryosphere, 16, 3531–3573, https://doi.org/10.5194/TC-16-3531-2022, 2022.

Van Leeuwen, P. J.: Particle filters for the Geosciences, Tech. rep., Data Assimilation Research Centre DARC, University of Reading, Reading, UK, 2012.

Vögeli, C., Lehning, M., Wever, N., and Bavay, M.: Scaling Precipitation Input to Spatially Distributed Hydrological Models by Measured Snow Distribution, Frontiers in Earth Science, 4, 108, https://doi.org/10.3389/feart.2016.00108, 2016.

Webster, C., Ginzler, C., Marty, M., Nussbaumer, A., Mazzotti, G., and Jonas, T.: Hourly potential light availability maps at 10 m resolution over Switzerland, Scientific Data, 12, 1882, https://doi.org/10.1038/s41597-025-06152-9, 2025.

Winstral, A., Magnusson, J., Schirmer, M., and Jonas, T.: The Bias-Detecting Ensemble: A New and Efficient Technique for Dynamically Incorporating Observations Into Physics-Based, Multilayer Snow Models, Water Resources Research, 55, 613–631, https://doi.org/10.1029/2018WR024521, 2019.

https://doi.org/10.5194/egusphere-2026-2725
Preprint. Discussion started: 27 May 2026

Zängl, G., Reinert, D., Rípodas, P., and Baldauf, M.: The ICON (ICOsahedral Non-hydrostatic) modelling framework of DWD and MPI-M : Description of the non-hydrostatic dynamical core, Quarterly Journal of the Royal Meteorological Society, 141, 563–579, https://doi.org/10.1002/qj.2378, 2015.